Positronium laser cooling in a magnetic field

Christian Zimmer, Pauline Yzombard, Antoine Camper, Daniel Comparat

▶ **To cite this version:**

Christian Zimmer, Pauline Yzombard, Antoine Camper, Daniel Comparat. Positronium laser cooling in a magnetic field. Physical Review A, 2021, 104 (2), 10.1103/physreva.104.023106 . hal-03369929

HAL Id: hal-03369929
https://hal.science/hal-03369929

Submitted on 7 Oct 2021

HAL is a multi-disciplinary open access archive for the deposit and dissemination of scientific research documents, whether they are published or not. The documents may come from teaching and research institutions in France or abroad, or from public or private research centers.

L'archive ouverte pluridisciplinaire **HAL**, est destinée au dépôt et à la diffusion de documents scientifiques de niveau recherche, publiés ou non, émanant des établissements d'enseignement et de recherche français ou étrangers, des laboratoires publics ou privés.

Positronium laser cooling in a magnetic field

Christian Zimmer,[1,2,3,4,*] Pauline Yzombard,[5,*] Antoine Camper,[4] and Daniel Comparat[6]

[1]*Physics Department, CERN, 1211 Geneva 23, Switzerland*
[2]*Department of Aerospace Science and Technologies, Politecnico di Milano, Italy*
[3]*Department of Physics, Heidelberg University, Im Neuenheimer Feld 226, 69120 Heidelberg, Germany*
[4]*Department of Physics, University of Oslo, Sem Saelandsvei 24, 0371 Oslo, Norway*
[5]*Kastler Brossel Laboratory, Sorbonne Université, CNRS, ENS Université PSL, Collège de France, 4 Place Jussieu, Case 74, 75252, Paris Cedex 05, France*
[6]*Université Paris-Saclay, CNRS, Laboratoire Aimé Cotton, 91405 Orsay, France*

(Received 30 April 2021; accepted 28 July 2021; published 18 August 2021)

We study realistic 3D laser cooling of positronium (Ps) in the presence of a magnetic field. Triplet and singlet states mixing due to the magnetic field, and dynamical Stark effect, generally produce higher annihilation rates than in the zero-field case. 3D cooling is efficient only at very low field $B \lesssim 50$ mT and at high field values $B \gtrapprox 0.7$ T. Near 100 ns long laser pulses, spectrally broad enough to cover most of the Ps Doppler profile and with energy in the mJ range, are required to cool Ps. Simulations based on full diagonalization of the Stark and Zeeman Hamiltonian and a kinetic Monte Carlo algorithm exactly solving the rate equations indicate that an efficient cooling (typically from 300 K down to below 50 K) is possible even in a magnetic field. We also propose 3D moving molasses cooling that can produce a well-defined monochromatic Ps beam useful for applications.

DOI: 10.1103/PhysRevA.104.023106

I. INTRODUCTION

Positronium (Ps), composed by an electron e^- and its antiparticle (e^+, a positron) is the lightest neutral atom that can be produced. It thus has very unique properties, similar to hydrogen, but it is purely leptonic (it contains no quarks). Hence, it became a testing ground for bound-state quantum electrodynamics. It is also an important tool for applied research, in particular, in porous condensed matter. Positronium physics and, in particular, Ps laser spectroscopy advanced rapidly in recent years (see Refs. [1,2] and references therein). Further progress in Ps spectroscopy and in Ps interaction with atoms and molecules will arise as soon as cold and dense Ps samples or a collimated beam of cold (and long lived) Ps atoms can be produced experimentally. This would enable direct applications such as interferometry with Ps [3,4], for instance, for gravity measurements [5] and for Ps spectroscopy experiments, and would open the way toward the creation of a Ps Bose-Einstein condensate (BEC) [6–13].

Clearly, one important step toward this direction would be laser cooling of Ps. The possibility of Ps laser cooling has been studied in Refs. [7,14–17]. From 2000 to 2002, the group of K. Wada, M. Kajita, and coworkers [8,18–21] experimentally proceeded to the first trials. Even if the laser development did not yield high enough energy per pulse for efficient cooling [18], numerical studies, modeling the cooling efficiency over the first transition $n = 1 \leftrightarrow n = 2$, were reported. In addition to the Doppler laser cooling, it has also been proposed to produce a BEC using thermalization with the nanochannels of a target converter and a Ps-Ps scattering process [6–13].

All these studies have been performed in a field-free environment. However, Ps is usually produced in a magnetic field environment, either to convey positrons toward the Ps formation target [2,22] or because they are used for antihydrogen experiments [23–25]. It has been suggested that high magnetic fields ($B > 2$ T) would be required for laser cooling to be efficient [26], but to our knowledge so far no numerical study has focused on Ps laser cooling in a magnetic field environment. This is the purpose of the present paper. We start with the specificity of Ps laser cooling in general in Secs. II and III. In Sec. IV, we discuss the mixing of the Ps electronic levels in the presence of a magnetic field (a Zeeman map is given in Fig. 1). We then report on simulations of the one- (Sec. VI), two-, and three-dimensional (Sec. VII) laser cooling cases and discuss the effects of both the magnetic field and the laser polarization. Finally, we conclude with a discussion on the feasibility of the experiment.

II. POSITRONIUM LASER COOLING CONSIDERATIONS

To study the feasibility of Doppler laser cooling of Ps atoms, one first has to take into account its limited lifetime: 142 ns for the ortho-positronium (o-Ps) and 125 ps for the para-positronium (p-Ps) in the ground state in free field.

[*]These authors contributed equally to this work.

Published by the American Physical Society under the terms of the Creative Commons Attribution 4.0 International license. Further distribution of this work must maintain attribution to the author(s) and the published article's title, journal citation, and DOI.

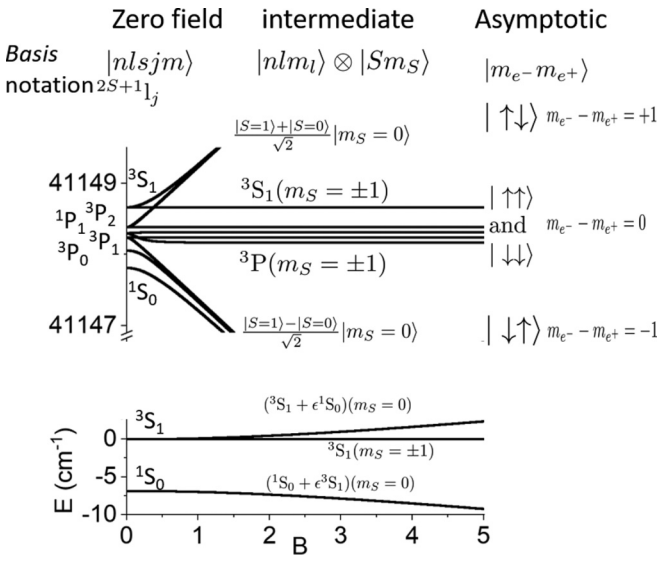

FIG. 1. Pure Zeeman effect from $B = 0$ to $B = 5$ T for the $n = 1$ and $n = 2$ manifolds. The levels are labeled in the $|nlsjm\rangle$ basis for zero field, in the $|nlm_l, Sm_S\rangle$ basis for intermediate fields, and in the $|nlm_l, s_{e^-} m_{e^-} s_{e^+} m_{e^+}\rangle$ basis for high fields using arrows for spin states: $\uparrow = 1/2, \downarrow = -1/2$. We also use the spectroscopic notation $^{2S+1}l_j$. For $n = 2$, the upper and lower branches are, for $B \gtrapprox 1$ T, in the Paschen-Back regime where the electron and positron spins are decoupled, creating superposition of singlet and triplet levels except for the flat branches where only pure triplet states exist. For $n = 1$, the field is not strong enough to reach the Paschen-Back decoupling regime and, except for the pure and flat triplet (with $m_S = \pm1$) branch, the $m_S = 0$ singlet and triplet branches show increasing coupling [indicated by the value of $\epsilon(B)$].

This short lifetime requires a fast and efficient laser cooling process, cycling only between triplet states (o-Ps), that lasts for a few tens of ns, whereas usual Doppler cooling, such as on alkali atoms, rather happens within several ms [27]. Based on this requirement, it has been suggested to laser cool Ps on the $1\,^3S_1 \leftrightarrow 2\,^3P_2$ transition, and simulations of this process are promising [14]. Indeed, the small mass ($m_{Ps} = 2 \times m_e$) of the Ps atom implies an important recoil energy for each absorbed or emitted photon, equivalent to a velocity kick of about $v_r = 1.5$ km/s or to a recoil temperature of $\frac{1}{2}mv_r^2/k_B = 0.15$ K. Potentially, in a few cycles of absorption and spontaneous emission, a great amount of energy can be dissipated. The light mass of Ps also presents some drawbacks, such as a significant Doppler effect. For instance, a Ps cloud with a root mean square 1D velocity of 1×10^5 m/s (equivalent to a temperature of 660 K), presents a Doppler broadening of about 400 GHz, much larger than the spontaneous rate of the $2P$ states $\Gamma = \frac{1}{3.2\,\text{ns}} \approx 2\pi \times (50\,\text{MHz})$. Nevertheless, simulations with a ∼100 GHz large laser bandwidth (to cover the Doppler broadening, but also for being able to address all $n = 2$ states, referred to as $2^3P_{J=0,1,2}$), a detuning in the tens of GHz range, a power of a few kW (corresponding to ∼1 mJ for a ∼100 ns long pulse), and a laser spot size of a few mm (which is the distance traveled by the Ps atoms during this time) suggest that it should be possible to observe laser cooling of Ps in a zero-field environment [7,14,24,28].

Yet the situation is more complex in the presence of a magnetic field, first because of the Zeeman splitting (cf. Fig. 1) but also because the high velocities of the Ps atoms create a motional Stark effect due to the $\boldsymbol{v} \wedge \boldsymbol{B}$ electric field that couples the S($m_l = 0$) and P($m_l = \pm1$) states. Furthermore, the values of magnetic field needed to reach the Paschen-Back regime are very different for $n = 2$ (for which a ∼1 T field seems to be large enough to decouple the electron and positron spins) and for $n = 1$ where at 5 T the upper branch is still far from being in a pure $m_{e^-} - m_{e^+} = 1$ state. The benefits of the strong field regime for Ps laser cooling will be treated in further detail in Sec. VI C. Since the annihilation and spontaneous emission dynamics of Ps atoms are affected by Stark and Zeeman mixing, laser interaction in the presence of a magnetic field can result in the decay of the atoms to the $m_S = 0$ ground states where a fast annihilation occurs, preventing any laser cooling to be applied if not carefully designed.

The evolution of the velocity distribution of Ps atoms over time is affected both by the laser-Ps interaction and by annihilation itself. An important parameter of this study is therefore the precise moment t_{exp} when the cold ensemble of Ps atoms should be ready for the foreseen application (e.g., antihydrogen production or atomic interferometry) to take place.

The present paper aims at giving key parameters to implement Doppler laser cooling schemes in various B field conditions [29–31], with a particular focus on the dynamics of the cooling process.

III. WHICH STATES SHOULD WE EXCITE?

In this paper, the system is restricted to $n = 1$ and $n = 2$ manifolds. For each state of the two manifolds, photoionization and annihilation rates are introduced to account for these two sources of loss. Laser cooling using the states of these two manifolds is more efficient than other cooling schemes involving higher n states because $n = 2$ has the shortest spontaneous emission lifetime of all excited states of Ps.

The system is described by rate equations [see Eq. (D1) of the Appendix for more details] governing the evolution of P_j, the population of state j with annihilation rate Γ_j^{ann} and photoionization rate Γ_j^{pi}. We note $\Gamma_{i\leftarrow j}$ and γ_{ij}, respectively, the spontaneous and stimulated emission rates from state j toward an individual state i. The rate equations can be written in a matrix form for the excited (e) (the 16 $n = 2$ levels) and ground (g) (the four $n = 1$ levels) manifolds, as

$$\frac{d}{dt}\begin{pmatrix} P_e \\ P_g \end{pmatrix} = \begin{pmatrix} -\Gamma_e^{loss} & \gamma^\dagger \\ \gamma + \Gamma & -\Gamma_g^{loss} \end{pmatrix}\begin{pmatrix} P_e \\ P_g \end{pmatrix}, \tag{1}$$

where the decay matrices $\Gamma_e^{loss} = \Gamma_e^{ann} + \Gamma_e^{pi} + \Gamma_e + \gamma_e$, $\Gamma_g^{loss} = \Gamma_g^{ann} + \Gamma_g^{pi} + \gamma_g$ are diagonals. The jth matrix element of Γ_e is $\Gamma_{e;j} = \sum_i \Gamma_{i\leftarrow j}$ and the ith matrix element of γ_g is $\gamma_{g;i} = \sum_j \gamma_{ij}$. To optimize the laser cooling strategy and remove the maximum momentum from the atomic motion, we try to maximize N_{scat}, the number of photons scattered during the laser-Ps interaction. N_{scat} is a good figure of merit for the efficiency of the laser cooling process. For an infinite

cooling time, this number is

$$N_{\rm scat} = \sum_j \Gamma_{{\rm e};j} \int_0^\infty P_j = {\rm Tr}\left[\Gamma \int_0^\infty P_{\rm e}\right]. \tag{2}$$

Throughout the paper, we assume no initial population in excited states, equally populated 1^3S states, and constant laser intensity during the whole interaction time. The block matrix inversion of Eq. (1) leads to $\int_0^\infty P_{\rm e} = [\Gamma_{\rm e}^{\rm loss} - \gamma^\dagger {\Gamma_{\rm g}^{\rm loss}}^{-1}(\gamma + \Gamma)]^{-1}\gamma^\dagger {\Gamma_{\rm g}^{\rm loss}}^{-1} P_{\rm g}(0)$. Because of annihilation, it is in general not obvious to determine the laser parameters (the γ matrix) that maximize $N_{\rm scat}$. To gain insight into the influence of annihilation on the laser cooling process, we first look at the simplest system, the two-level case with one ground and one excited state. To separate the two effects and focus on annihilation, we momentarily (only for this two-level case) neglect photoionization. In this case, the highest possible laser intensity ($\gamma \to \infty$) maximizes $N_{\rm scat}$ to

$$N_{\rm scat} = \frac{\Gamma}{\Gamma_{\rm e}^{\rm ann} + \Gamma_{\rm g}^{\rm ann}}. \tag{3}$$

Equation (3) suggests that $N_{\rm scat}$ can be increased by exciting a level with slow annihilation $\Gamma_{\rm e}^{\rm ann}$ and fast spontaneous emission Γ rates which also decays toward a long-lived state (small $\Gamma_{\rm g}^{\rm ann}$). This again highlights the fact that the singlet part of the ground state should not be populated during the cooling process and that the choice of the $n = 2$ manifold is wise, because the $2P$ states have the smallest spontaneous emission lifetime among all Ps energy levels. Using a triplet ground state and exciting to a $2P$ state which has an annihilation lifetime on the order of, or higher than 100 µs (formulas are recalled in Appendix A), leads to $N_{\rm scat} = \frac{142\,{\rm ns}}{3.2\,{\rm ns}} \approx 45$ photons. Thus, with the recoil velocity $v_{\rm r} = \frac{\hbar k}{m} \approx 1500\,{\rm m/s}$, it comes that the velocity can be modified by $\approx$70 km/s.

By studying numerically simple three- and four-level systems, we confirm the findings of the simple two-level system: an important parameter is to select an excited state for which the spontaneous emission rate toward a level i ($\Gamma_{i\leftarrow {\rm e}}$) is bigger than the annihilation rate of the state i ($\Gamma_i^{\rm ann}$). Let us consider a practical example. For $B = 1.5\,{\rm T}$, the two $m = 0$ ground states are mixed, but one is still mainly of triplet character (as illustrated in Fig. 1, this state is a superposition of $1^1S, m = 0$ and $1^3S, m = 0$). However, the annihilation lifetime of this state is drastically shortened and equal to the spontaneous emission lifetime of the $2P$ state. This implies that only one or two photons could be scattered on the transition involving the $m = 0$ ground state before annihilation of the Ps occurs, precluding any cooling process. Therefore, for a magnetic field $B > 1.5\,{\rm T}$, the laser pulse should be designed to avoid populating the $m = 0$ ground states even if one of them is still mainly of triplet character.

Another interesting aspect is that it may be advisable to laser excite several states (provided that they have small annihilation rates) because this increases the dressed state system annihilation lifetime and the overall cycling time. As an extreme toy example, in zero field, if it were possible to saturate all triplet states, i.e., the three ground 1^3S and the nine excited $2^3P_{J=0,1,2}$ levels to equalize individual level population, the number of scattered photons from Eq. (2) would become $N_{\rm scat} = \frac{9}{3}\frac{142\,{\rm ns}}{3.2\,{\rm ns}} \approx 133$ photons. This would allow better cooling than cycling between only two levels.

IV. ZEEMAN EFFECT AND DYNAMICAL STATE MIXING

We now recall some of the basic ingredients of the Ps Hamiltonian in presence of a magnetic field $\boldsymbol{B} = B\boldsymbol{u}_z$. All formulas for the transition dipole moments and for the Stark and Zeeman coupling are given in Appendix A. Here, only the main effects are presented to illustrate the reasoning that led to the choice of initial parameters for the simulation studies. We use obvious notations such as $|s_{e^-} m_{e^-}\rangle$ for the electron spin state with spin $s_{e^-} = 1/2$ and angular momentum m_{e^-}.

The main ingredients are the (singlet and triplet) character, the Zeeman and dynamical Stark coupling between these states as well as the energy broadening.

Because the orbital magnetic moments of the electron and positron cancel each other exactly, the (linear) Zeeman Hamiltonian $\hat{H}_{\rm Z}$ is diagonal in the individual, electron, and positron spin basis. Approximating the electron g_e factor to -2 and with the Bohr magneton $\mu_{\rm B} = \frac{e\hbar}{2m_e}$, $\hat{H}_{\rm Z}$ is given by

$$\hat{H}_{\rm Z}|m_{e^-} m_{e^+}\rangle = 2\mu_{\rm B} B(m_{e^-} - m_{e^+})|m_{e^-} m_{e^+}\rangle. \tag{4}$$

In addition, the total spin basis, leading to the singlet $S = 0$ and triplet $S = 1$ states description, can be defined by

$$\begin{aligned}
|S = 0\, m_S = 0\rangle &= \frac{1}{\sqrt{2}}(\,|\uparrow\downarrow\rangle - |\downarrow\uparrow\rangle),\\
|S = 1\, m_S = 1\rangle &= |\uparrow\uparrow\rangle,\\
|S = 1\, m_S = 0\rangle &= \frac{1}{\sqrt{2}}(\,|\uparrow\downarrow\rangle + |\downarrow\uparrow\rangle),\\
|S = 1\, m_S = -1\rangle &= |\downarrow\downarrow\rangle,
\end{aligned}$$

where, on the right-hand side of the equal signs, the individual spin basis states $|m_{e^-} m_{e^+}\rangle$ are represented by arrows $\uparrow = 1/2, \downarrow = -1/2$. In this basis, the eigenstates of the total spin $\mathbf{S} = \mathbf{s}_{\mathbf{e}^-} + \mathbf{s}_{\mathbf{e}^+}$ are the field-free states. For example, for the $n = 1$ manifold, the eigenstate with eigenvalue $S = 0$ is the para-positronium (p-Ps with an annihilation lifetime of 125 ps) and the eigenstates with eigenvalue $S = 1$ are the three triplet states of ortho-positronium (o-Ps with an annihilation lifetime of 142 ns for all three states). In this basis,

$$\hat{H}_{\rm Z}|S, m_S\rangle = 2\mu_{\rm B} B\, \delta_{0m_S}|1 - S, m_S\rangle, \tag{5}$$

where δ_{0m_S} is the Kronecker delta function.

In the $n = 1$ manifold, the two triplet $m_S = \pm 1$ levels are thus unaffected (as visible in Fig. 1) and keep an annihilation lifetime of 142 ns independently of the strength of the magnetic field. On the contrary, a magnetic field dramatically shortens the lifetime of the $m = 0$ o-Ps (triplet) level by coupling it to the p-Ps (singlet) $m = 0$ level [see Eq. (5)].

As highlighted by Eq. (3), the ratio between the spontaneous emission and the annihilation lifetimes is the pertinent parameter to understand the cooling efficiency. In Figs. 2(a) and 2(b), two color-coded Zeeman maps are given: One color code highlights the annihilation lifetime of the $n = 1$ levels, and only applies to the bottom part of each panel. A second color code (for the top part of each panel) gives a rough estimate of the number of scattered photons for each eigenstate

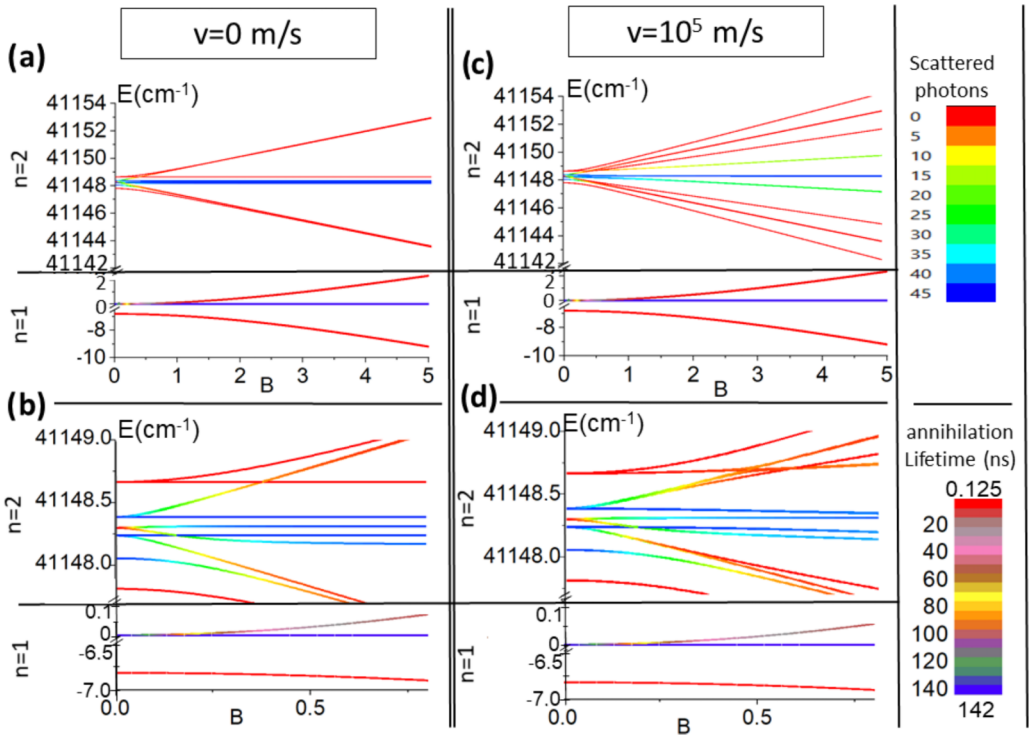

FIG. 2. Zeeman and dynamical Stark effect for Ps in a magnetic field B for values ranging from 0 to 5, in Tesla. Two extreme velocity (transverse to the magnetic field) cases are presented: $v_\perp = 0$ (a) [and a zoom in (b)] and $v_\perp = 1 \times 10^5$ m/s (c) [and a zoom in (d)]. For better separation of the curves, the vertical scaling (for the $n = 1$ manifold) is not always the same. A first color code gives the annihilation lifetime for the ground ($n = 1$) states. A second color code gives, for the excited ($n = 2$) states, a rough estimate of the number of photons that can be scattered (see Sec. IV).

j of the $n = 2$ manifold, defined as the sum over all ground states i of the ratio between the spontaneous emission lifetime and the annihilation lifetime: $N_{\text{scat}} \approx \sum_i \frac{\Gamma_{ij}}{\Gamma_j^{\text{ann}} + \Gamma_i^{\text{ann}}}$.

In $n = 2$, eight eigenstates (2 in ^3S and six in ^3P) with $m_S = \pm 1$ are insensitive to the Zeeman effect because $m_{e^-} = m_{e^+} = \pm 1/2$ [cf. Eq. (4)]. Therefore, the $^3P(m_S = \pm 1)$ excited states, which have no singlet component, are very good candidates for an efficient laser cooling scheme. The other eight $m_S = 0$ eigenstates have, at high magnetic field, energies shifted by $\pm 2\mu_B B$. These states are 50% singlet and 50% triplet. An efficient laser cooling scheme should avoid exciting these states. This can be done either by using selection rules linked to the laser polarization, which works mainly only in the 1D configuration, or by means of wavelength selection at high magnetic field where the states are well separated (Paschen-Back regime, where $\hat{\boldsymbol{L}}$ and $\hat{\boldsymbol{S}}$ are decoupled).

An important additional complexity arises due to the high Ps velocity. Indeed, an atom moving in a pure magnetic field sees an electric field given, in the nonrelativistic limit, by the Joules-Bernoulli equation: $\boldsymbol{E} = \boldsymbol{v} \times \boldsymbol{B}$. The atom is thus affected by a (motional) Stark effect $\hat{H}_S = e\hat{\boldsymbol{r}} \cdot \boldsymbol{E}$. This motional electric field is only due to the transverse component of the velocity $v_\perp$ (that is, v_x or v_y for $\boldsymbol{B}$ along z). It is orthogonal to the quantization axis defined by the magnetic field and $\hat{H}_S$ couples only $m_l = 0$ and $m_l = \pm 1$ states. Therefore, the only important contribution of the motional Stark effect is on the $n = 2$ manifold due to S and P mixing. In the $|n, l, m\rangle$ basis, $\langle 2, 0, 0|\hat{x}|2, 1, \pm 1\rangle = \mp i\langle 2, 0, 0|\hat{y}|2, 1, \pm 1\rangle = \mp 3\sqrt{2}ea_0^{(\text{Ps})}$, where e is the elementary charge and $a_0^{(\text{Ps})} = 1.05836 \times 10^{-10}$ m is the positronium Bohr radius. This leads to a matrix element for the Stark effect of 5 GHz for $v_\perp = 1 \times 10^5$ m/s and $B = 1$ T. This becomes visible in the Zeeman-Stark map of Fig. 2 by comparing 2(c) and 2(a). A net effect is that some of the pure flat triplet states $^3P(m_S = \pm 1)$ in a pure magnetic field with no transverse velocity considered (that can scatter 45 photons) are now (in the $v_\perp = 1 \times 10^5$ m/s case) mixed with the metastable ^3S level and the new eigenstates, when fully mixed in high fields, have a spontaneous emission lifetime of 6.4 ns which reduces the number of possibly scattered photons by a factor of 2.

V. SIMULATION TOOL

A. Rate equations code

It is beyond the scope of this paper to discuss experimental considerations such as the choice of the laser system. However, the latter can have implications on the tools required to simulate the cooling process. For instance, because of the large laser spectrum required to cover the Doppler spectrum and because of the benefits brought by spectral shaping, such as reaching subrecoil temperatures [14], one could think of using a femtosecond laser. With ultrashort pulses, coherent effects become important and Bloch equations are required to simulate the process. Very interesting (coherent) cooling methods can be investigated with such tools [32–36]. However, the required high intensity pulsed lasers are extremely

difficult to build and most of the developed or suggested laser systems for Ps laser cooling are incoherent broadband lasers such as the fourth harmonic of a Cr:LiSAF laser [20] or the third harmonic of a multipass Ti:sapphire laser [11]. For this purpose, a ∼40 GHz broad bandwidth and ∼500 ns long pulse duration Ti:Sa laser has been demonstrated very recently [37].

In the case of incoherent broadband lasers considered in the present paper, laser cooling of positronium can be properly simulated within the rate equations formalism [38]: The effect of cooling on the atoms can be derived by calculating the changes in momentum due to absorbed and scattered photons over time. We use this formalism to numerically simulate Ps laser cooling using a C++ code. The program diagonalizes the Hamiltonian in the presence of magnetic and dynamical Stark fields. The eigenvectors and eigenvalues are used to derive the external forces (scattering due to momentum recoil, dipolar, magnetic, and gravity). External motion is taken into account using a Verlet algorithm. The internal state evolution due to absorption, spontaneous and stimulated emissions is described by the rate equations which are solved by means of a kinetic Monte Carlo (KMC) algorithm with fixed time steps of 500 ps. Some parts of the program have already been exposed in Ref. [38,39]. More details and generalizations can be found in Appendixes B–D.

In addition to the 20 levels (4 in $n = 1$ and 16 in $n = 2$), five dead levels (with $m = -2, -1, 0, 1, 2$) are added to include the annihilation treated as a π polarized spontaneous decay toward these levels. Seven additional continuum levels (with $m = -3, -2, -1, 0, 1, 2, 3$) are included to account for photoionization, which is treated as a polarization-dependent excitation toward these levels by using dipoles based on the photoionization cross sections. This allows us to only use dipolar transitions to treat all phenomena (spontaneous emission, absorption, stimulated emission, annihilation, and photoionization) as explained in-depth in Appendix D 1. The strength of these phenomena is known in zero field. To calculate their values for nonzero fields, we diagonalize the Hamiltonian including the Zeeman and dynamical Stark effect. Standard rotation is applied to account for the different axes: the laser propagation, the polarization, and the fields' axes. We check that the Zeeman effect does not induce any energy level crossing in the ground state, which makes it easy to keep track of the (energy) levels during the quasirandom spontaneous emission step. Note that the calculation of the annihilation and photoionization rates are incoherent but all the other dipole transitions calculations are coherent.

One major difficulty with solving rate equations by means of a KMC algorithm (especially for 3D systems), relates to the fact that the diagonalization procedure is not unique. As a result, the eigenvectors are arbitrarily defined which results in uncontrolled coherent phases between the states. This coherence is not taken into account by the incoherent rate equation system. This may have important implications that we want to illustrate on a toy example with a pure magnetic field σ^+ transition between $1\,^3S_1(m = 1) \leftrightarrow 2\,^3P_2(m = 2)$. If the population is initialized in $m = 1$, this is (in pure magnetic field) a closed transition and so no $1\,^3S_1(m = -1)$ level is populated. However, the $2\,^3P_2(m = +2)$ level is degenerated in energy with the $2\,^3P_2(m = -2)$ one. So the diagonalization process might choose, as eigenstates, the $|\pm\rangle = (|m = +2\rangle \pm |m = -2\rangle)/\sqrt{2}$ states. Therefore, the σ^+ transition starting from $1\,^3S_1(m = 1)$ will excite both $|-\rangle$ and $|+\rangle$ states. However, by construction, there is no superposition of states in rate equations, thus, the KMC algorithm will choose (with a probability linked to the dipole transition strength, hence here with 50% chance each) to populate only one level after the excitation, for instance, the $|+\rangle$ level. Then the $|+\rangle$ level can decay, by spontaneous emission in the $1\,^3S_1(m = -1)$ level. This example illustrates how a rate equation code might produce the wrong physical results. In our case, this mixing behavior is observed for specific rotations and specific laser polarization states. This basis problem is inherent to incoherent rate equations. To avoid this, we add a small energy shift (typically $10^{-5}\,\mathrm{cm}^{-1}$) to prevent any energy degeneracy in zero field. However, when the Zeeman and dynamical Stark effects are included, the evolution of these coherent phases cannot be trivially predicted. Using a large enough atomic sample, this mixing effect can be mitigated and averaged out due to the multiple possible initial atomic directions and, especially in 3D cooling, due to different laser polarizations. This effect results in an artificial limitation of specific optical pumping scheme efficiencies. Tests conducted with different diagonalization algorithms producing different phases yielded similar results. Therefore, we are confident that the results presented here are not significantly affected by this effect, although special care has to be taken to draw conclusions when polarization is involved.

B. Ps laser cooling parameters

Several parameters have to be defined: the Ps temperature, the Ps cloud size, the laser power, detuning, polarization and spectrum, the magnetic field value, and orientation. To get insight into this multivariate space, we first study the 1D-cooling case before turning to the more complex 2D and 3D cooling.

We consider two typical ways of producing Ps. First, Ps can be formed by charge exchange with a plasma of positrons [23,40]. In this case, the ensemble of Ps atoms is well represented by a 3D expanding cloud with Gaussian velocity distribution and zero mean velocity along each spatial direction. This is similar to a 3D molasses or magneto-optical trap simulation and has been used for all Ps numerical laser cooling studies before. This is also the case considered in Sec. VI. However, Ps can also be created by implantation of positrons in a converter target. In this geometry, it is mostly emitted in the forward direction (orthogonal to the target) [2,41] with a nonzero mean velocity and the Ps cloud is thus similar to an effusive beam. This case is investigated in Sec. VII B.

To evaluate the cooling efficiency of the different configurations, we define an N-particle effective temperature T_i along the i axis. For this calculation, we take into account only 50% of all atoms, namely, those from the second and third quartiles of the velocity distribution along i (i.e., those with smallest absolute velocities v_i) and ignore the remaining 50% with extreme velocities. T_i is defined as

$$\frac{1}{2}k_B T_i = \frac{1}{\chi}\frac{1}{N/2}\frac{1}{2}m\sum_{j\leqslant N/2}(\bar{v}_i - v_{i,j})^2, \tag{6}$$

where $v_{i,j}$ is the velocity of particle j along axis i, m is the mass of a Ps atom and $\bar{v}_i = \frac{1}{N/2}\sum_{j\leqslant N/2} v_{i,j}$ is the mean ve-

locity along i of all the $N/2$ particles with the slowest absolute velocity along axis i.

$$\chi = \int_{v_i^{25}}^{v_i^{75}} dv_i \frac{e^{-\frac{v_i^2}{2\sigma^2}}}{\sqrt{2\pi}\sigma} \frac{\frac{1}{2}mv_i^2}{\frac{1}{2}k_B T} \approx 0.142652$$

is a normalization factor to recover the usual temperature T of a Maxwellian velocity distribution. v_i^{25} is the first (lower) quartile and v_i^{75} the third (upper) quartile for the velocity distribution along axis i. In complement to T_i, we introduce a second figure of merit for the cooling efficiency which is n_r, the number of Ps atoms with velocity in the range of two times the recoil velocity, $|v_i| \leqslant 2v_r$. For additional insight, n_r is evaluated with $[n_r(\mathrm{ON})]$ and without $[n_r(\mathrm{OFF})]$ the laser-cooling pulse. The comparison between $n_r(\mathrm{ON})$ and $n_r(\mathrm{OFF})$, enabled by the $S = \frac{n_r(\mathrm{ON}) - n_r(\mathrm{OFF})}{n_r(\mathrm{OFF})}$ parameter, highlights the effect of the laser pulse on n_r for a given set of parameters.

A discussion of the laser parameters is presented in Sec. VI B. The first simulations assume a laser spot size on the order of 1 cm diameter (meaning a waist w of 5 mm), for a pair of counterpropagating beams with a Gaussian spectral bandwidth Γ_L (FWHM) of 75 GHz, a detuning δ of $-2.5\,\mathrm{cm}^{-1}$ (that is, -75 GHz) from resonance $E_0 = \hbar\omega_0$ (for which we choose the transition $1\,^3S_1 \leftrightarrow 2\,^3P_1$ at 41148.23871 cm^{-1}) and a laser power of 2 kW. This corresponds to an energy of 400 μJ per laser pulse during the whole simulation time of $t = 200$ ns (or 240 μJ for 120 ns). This time span has been chosen as a compromise between the annihilation lifetime of 142 ns, the traveling time of the atoms through the laser waist, and realistically achievable laser pulse duration. In all 1D simulations, the cloud is initialized instantaneously in time and with a Gaussian distribution of 0.1 mm waist along each of the three spatial directions.

VI. 1D COOLING

In this section, 1D laser cooling on a (nonmoving) 3D expanding cloud of Ps is investigated. All 1D-cooling simulations have been carried out for a cloud of 2000 Ps atoms which is expanding isotropically in 3D with thermal velocities corresponding to a realistic experimental temperature of $T = 300$ K [2]. This number of atoms is chosen as a compromise between computational time and sampling density of the velocity distribution. In all simulations, when the number of annihilated atoms is high, the results have lower statistical significance. However, this does not affect the conclusions of the studies presented in this paper which are based on statistically significant results.

We first present a detailed study of longitudinal cooling (laser along the magnetic field) with circular polarization for typical laser parameters, then we explore a range of laser parameters in 1 T, and, finally, scan the value of the magnetic field for fixed laser parameters. The initial population of Ps is initialized such that all three triplet ground states are populated equally in all simulations.

A. 1D-cooling dynamics

To limit the effects of the Zeeman mixing on laser cooling, the σ^+-σ^+ configuration can be used to cycle on the $1\,^3S_1(m=1) \leftrightarrow 2\,^3P_2(m=2)$ states that do not mix in a pure magnetic field [see Figs. 2(a) and 2(b)]. In this configuration, the two laser beams propagate along the z axis which is also the axis of magnetic field ($\boldsymbol{B}$ along z). The polarization of the lasers is in the σ^+-σ^+ configuration (one left- and one right-circular polarization).

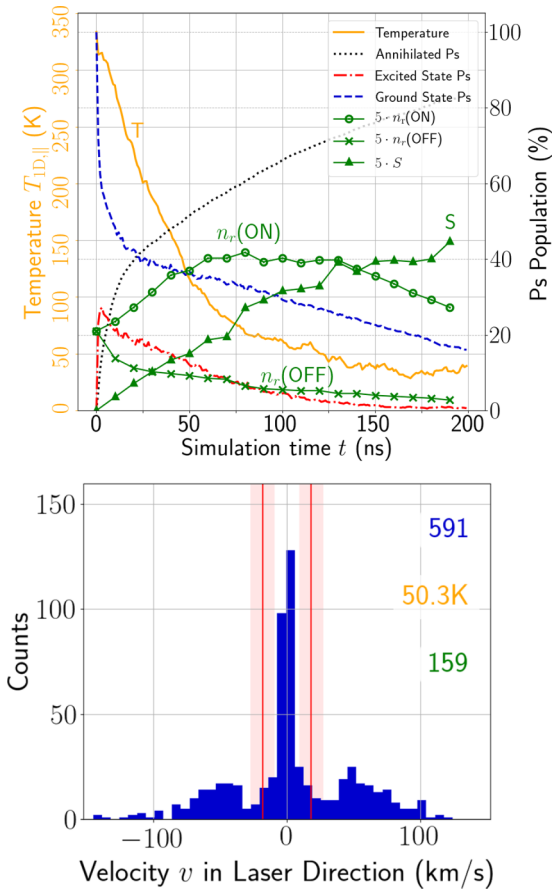

FIG. 3. 1D laser cooling of a 3D expanding cloud of $N = 2000$ Ps atoms. The laser parameters of $\Gamma_L/(2\pi) = 75$ GHz, $\delta = -2.5\,\mathrm{cm}^{-1}$ and $P = 2$ kW have been used. The magnetic field $\boldsymbol{B}$ and the lasers are along z. Lasers are circularly polarized. Top: Evolution of T_z (orange, solid line), the percentage of annihilated Ps (black, dotted) and of the Ps population in ground (blue, dashed) and excited states (red, dash-dotted). The green line in –o– style gives the percentage $n_r(\mathrm{ON})/N$ of Ps around $v = 0$ for the laser ON case, the one in –x– style $n_r(\mathrm{OFF})/N$ for laser OFF, and the one with triangles shows $S = [n_r(\mathrm{ON})\text{-}n_r(\mathrm{OFF})]/n_r(\mathrm{OFF})$, representing the percentage of gain of the laser ON case compared to laser OFF, all scaled by a factor of 5 for the sake of visibility. Bottom: Histogram of the v_z distribution at $t = 120$ ns. For illustration purposes, the red lines show the spectral position of the laser light in terms of detuning δ with respect to resonance and the transparent areas indicate the laser (FWHM) bandwidth Γ_L. The blue numbers indicate the number of nonannihilated atoms, the orange ones the according final value of T_z, and the green ones give n_r at $t = 120$ ns.

Figure 3 presents the results of these simulations, including the evolution over time of T_z, $n_r(\mathrm{ON})$, $n_r(\mathrm{OFF})$, S, and the population in different states as well as histograms of the final distributions of the Ps velocity component along the laser direction. Only 1 Ps among the 2000 atoms is photoion-

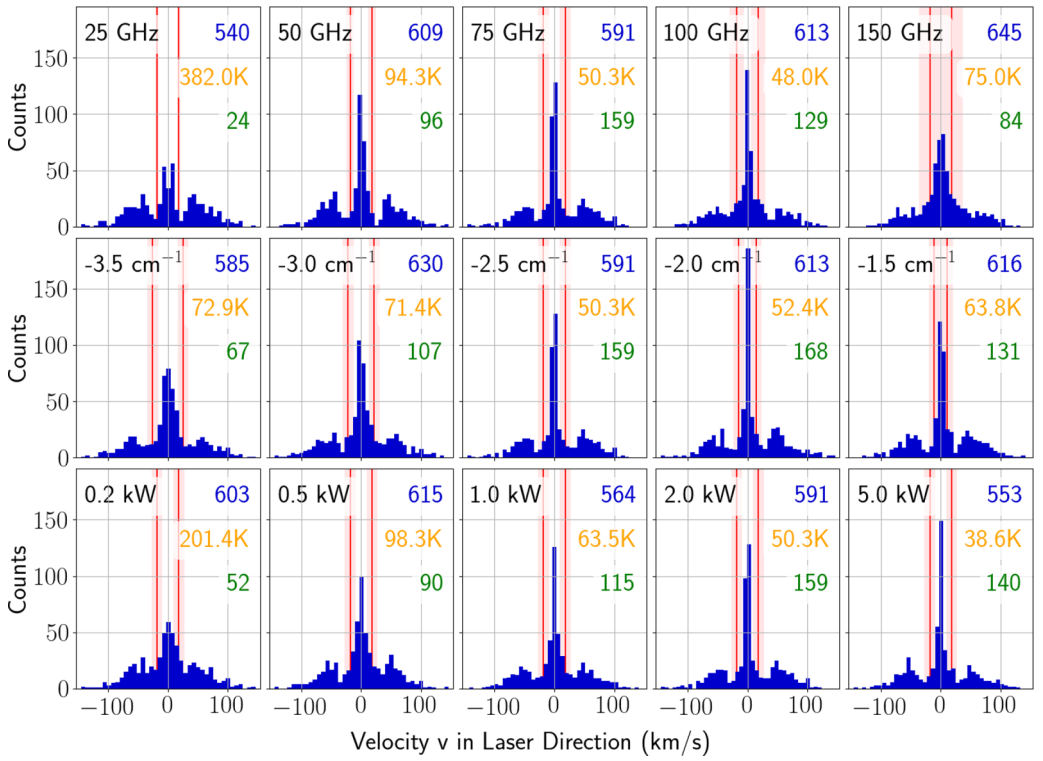

FIG. 4. Laser parameter scans in $B = 1\,\mathrm{T}$ for 1D longitudinal cooling. Histograms of the Ps velocity component along the laser direction z after 120 ns for the three laser parameters' bandwidth Γ_L (first row), detuning δ (second row), and power P (third row). Notations are similar to Fig. 3 with all numbers referring to 2000 Ps atoms. If not scanned, the parameters are $\Gamma_\mathrm{L}/(2\pi) = 75\,\mathrm{GHz}$, $\delta = -2.5\,\mathrm{cm}^{-1}$ and $P = 2\,\mathrm{kW}$.

ized, which suggests that photoionization can be neglected in this range of laser power. Indeed, a 243 nm 10 kW laser, with a $1\,\mathrm{cm}^2$ uniform spot size, and 200 ns pulse duration, photoionizes only 0.4% of the $(2P)$ atoms (using the cross sections given in Appendix A: $\sigma_{n=2,l=1}^{k=0.71,l'=2} + \sigma_{n=2,l=1}^{k=0.71,l'=0} = 1.5 \times 10^{-22}\,\mathrm{m}^2$).

The first important result is that S constantly increases over the entire 200 ns window, demonstrating that the cooling laser allows one to increase the number of cold atoms compared to a situation without laser excitation.

A second noticeable feature is the initial sudden rise of the excited states population (red dash-dotted curve), which reaches a peak within a few nanoseconds and then slowly falls. This is the expected behavior for a saturated excitation: a high fraction of the atoms are excited within the first instants of the laser-Ps interaction. This, combined with the rapid annihilation of the singlet states, explains the initial sudden fall in the population of the ground state (blue dashed curve) which, however, does not reach a linear regime until about 20 ns, much later than the time when the population in the excited states peaks. This excess of loss in the ground state can be linked to the reduced annihilation lifetime (6.7 ns for $B = 1\,\mathrm{T}$) of the $m = 0$ ortho-Ps mixed with para-Ps.

Another general observation linked to the previous one is that, after 200 ns, the fraction of annihilated Ps atoms (nearly 85%) in a 1 T field is higher than the 70% observed in similar field-free environment simulations (see the case $B = 0\,\mathrm{T}$ in Fig. 5). This rise is expected because of the presence of the magnetic field which leads to magnetic quenching and internal state mixing induced by the Zeeman effect.

In conclusion of this first study: cooling can occur mainly on transitions involving long-living m states despite the Zeeman and motional Stark mixing, allowing long cooling interaction times with a relatively limited enhanced annihilation rate (after a first period of fast annihilation of the $m = 0$ initial states). If the phase loss issue resulting from the diagonalization of the Hamiltonian (see Sec. V A) has any effect on the results presented in this section, it is only to reduce the efficiency of the cooling process by artificially populating fast annihilating states that in reality are not populated when using this scheme.

B. Laser parameter scans for 1D-cooling in 1 T

In this section, we keep the σ^+-σ^+ configuration described in Sec. VI A and scan the laser power, bandwidth, and detuning separately. The resulting longitudinal velocity distributions $t = 120\,\mathrm{ns}$ are presented in Fig. 4. When not scanned, the parameters are set to the following default parameters: $P = 2\,\mathrm{kW}$ (the laser power), $\Gamma_\mathrm{L}/(2\pi) = 75\,\mathrm{GHz}$ (the FWHM bandwidth corresponding to a standard deviation of about $\sigma/(2\pi) = 32\,\mathrm{GHz}$ for a Gaussian laser spectrum), $\delta = -2.5\,\mathrm{cm}^{-1}$ (the detuning corresponding to $-75\,\mathrm{GHz}$), and $w = 5\,\mathrm{mm}$ (the laser waist). The cloud, which contains 2000 Ps atoms at $t = 0\,\mathrm{ns}$, is always initialized at a temperature of 300 K and such that the initial population is distributed equally over all three ground states.

From the results displayed in Fig. 4, apart from extreme values of the scanned parameters, efficient laser cooling is observed for all considered configurations: the number n_r

of slow atoms within the $\pm 2 \times v_r$ velocity range is always higher after 120 ns of laser-Ps interaction, compared to the situation with no laser and to its value at $t = 0$ ns. All velocity histograms shown in Fig. 4 present an important peak centered at $v_z = 0$, surrounded by two depleted classes of velocity (the laser-cooled velocity range, selected by the laser detuning, bandwidth, and power). This is the result of momentum transfer toward lower velocities. The height and width of these peaks reflect the efficiency of laser cooling using different sets of laser parameters.

One important parameter to maximize the cooling efficiency is the laser bandwidth, which should be large enough to cover most of the Doppler broadening of the Ps cloud but not too wide in order to avoid exciting also the atoms in the zero-velocity class. This is shown in the first row of Fig. 4, where we can see how the structure of the velocity distribution changes with the laser bandwidth: when it is too narrow, the capture range is too small to cool a large part of the atoms. As a consequence, two center peaks build up symmetrically around $v_z = 0$ instead of accumulating atoms in the $v_z = 0$ range. This is because the middle-range velocity class is not addressed by the laser, which is too far detuned and too narrow to excite them and cool them down to the $v_z = 0$ range. On the other hand, when the laser is too broad, the depletion becomes less and less pronounced and the central peak gets damped, as even the zero-velocity atoms can be at resonance with this large laser and get a momentum transfer to kick them out the zero-velocity range.

The results of the detuning scan are plotted in the second row of Fig. 4. As expected, when the laser detuning matches approximately the Doppler width (between $\delta = -3.0\,\mathrm{cm}^{-1}$ and $\delta = -2.0\,\mathrm{cm}^{-1}$) and the laser bandwidth takes roughly the same value ($\Gamma_L/(2\pi) = 75$ GHz), the cooling effect is strongest. In the rest of the paper, the detuning is set at its $-2.5\ \mathrm{cm}^{-1}$ optimum for a Ps cloud of 300 K initial temperature.

The last scan of this section aims at optimizing the laser power. We define the saturation parameter s (for broadband lasers) and saturation intensity I_{sat} as

$$s = \frac{I_L}{I_{sat}} \frac{\Gamma}{\Gamma + \Gamma_L}, \quad I_{sat} = \frac{1}{6}\hbar c \left(\frac{2\pi}{\lambda}\right)^3 \frac{\Gamma}{2\pi},$$

where Γ_L is the laser bandwidth, $\Gamma = 1/3.2$ ns is the spontaneous emission rate, $\lambda = 243$ nm and $I_L = \frac{2P}{\pi w^2}$ the laser intensity corresponding to an excitation rate of $\gamma = 1/1.7$ ns (see Appendix B). The range of laser power explored in the simulation covers from below saturation ($s < 1$) to well into the saturation regime ($P = 5$ kW corresponds to $s \sim 20$). The results presented in the third row of Fig. 4 suggest that a power of 2 kW, leading to a moderate saturation regime ($s \sim 8$), is a good compromise between higher final number of atoms and reasonable laser power.

From these scans, we conclude that there is a range of laser parameters yielding similar laser cooling efficiency for which the initial temperature T_z is reduced by a facto of 4 at $t = 120$ ns and $n_r \approx 160$, which represents an increase of 100% compared to the initial value of $n_r \approx 80$.

One important effect limiting the achieved temperature is the fact that Ps atoms move so fast that they can escape the Ps-laser interaction area during the cooling time. Consequently, cooling the majority of the Ps atoms requires a large enough beam waist to continue interacting with the moving Ps during the whole pulse duration. As a consequence, the ideal laser power required to cover spatially the Ps cloud during ~100–200 ns is relatively high. This is an experimental limitation to overcome. In the simulations presented here, we opted for a large 5 mm laser beam radius (waist), 2 kW power, and 200 ns pulse duration that seems to us a realistic choice for future experiments. However, with a 10 mm laser waist and 8 kW power, the number of slow Ps (n_r) after a 120 ns laser interaction time is typically 10% higher than for the 5 mm interaction region, reaching 180 atoms instead of 160 atoms. As expected, the laser power has to be optimized when changing the geometry of the setup (Ps and laser initial waists). In the rest of the paper, except if specified differently, the simulations are run with the following optimized values (for a laser $w_L = 5$ mm): $\Gamma_L/(2\pi) = 75$ GHz, $\delta = -2.5\,\mathrm{cm}^{-1}$, and $P = 2$ kW.

C. Dependence of 1D-cooling performance on the magnetic field strength

Finally, to study the influence of the magnetic field strength on the cooling performance, we carry out simulations where the B field value is scanned between 0 and 5 T. We did not optimize all laser parameters for each B value, but we checked on a few ones that, if some precise numbers are affected, this does not change the overall discussion.

The results are shown in Fig. 5, which contains the 1D temperature (T_z in orange) as well as the population in different state categories ($n = 1$ in dashed blue, $n = 2$ in dash-dotted red, and the annihilation percentage in dotted black) and in the slow velocity range (n_r, in green "-o–o–line style). The top part of Fig. 5 summarizes the results at $t = 120$ ns as a function of the magnetic field scanned in steps of 0.03 T from 0 to 1 T and in steps of 0.1 T from 1 to 5 T. The bottom part of the figure features a zoom-in at three magnetic field values of interest: zero-field, low-field (0.3 T) and high field regions (1 T) corresponding to the Paschen-Back regime for $n = 2$.

The most interesting observation is the development of T_z at $t = 120$ ns as a function of the magnetic field. Considering this figure of merit, cooling becomes completely senseless for B between ~0.1 T and 0.7 T where the final estimated temperature exceeds the initial 300 K. This rise results from the fast annihilation of laser-excited atoms that are mixed with short-living states due to Zeeman and motional Stark mixing, so only the nonexcited faster atoms remain alive and contribute to the temperature calculation. However, we emphasize that the number of slow atoms (n_r) within the range of interest ($\pm 2v_r$) is yet higher than for the no-laser case, even in the low-field region, thanks to the polarization cycling with σ^+ polarization, discussed in Sec. VI A.

To zoom in on the different results revealed here, we first focus our discussion on the zero-field case for later comparison. For $B = 0$ T, we verify that a bit more than 25% of the atoms are excited to $n = 2$ in the first instants of interaction, which corresponds to the observed 25% drop in the ground state population. This drop is thus not due to any fast annihilation mechanism as in the nonzero magnetic

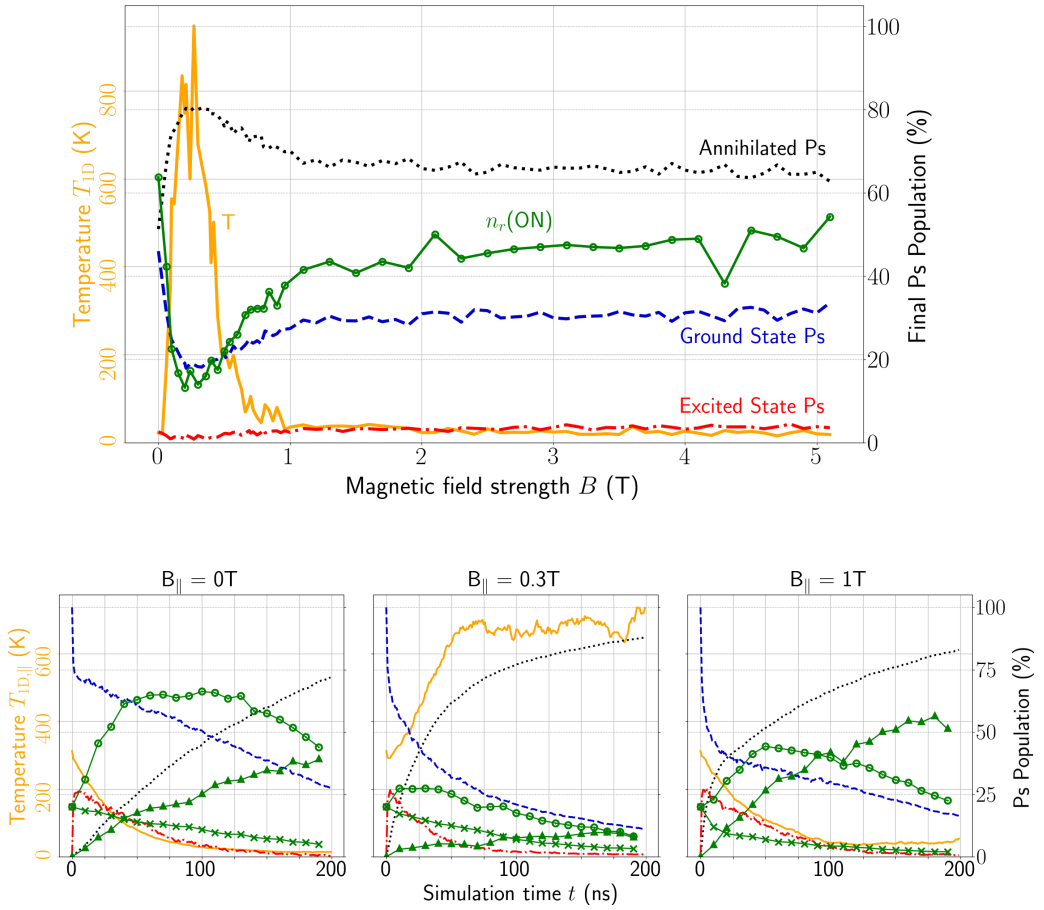

FIG. 5. Ps cooling efficiency versus magnetic field strength. Top: The left axis indicates the final 1D temperature (T_z at $t = 120$ ns, orange) and the right axis the final fraction of annihilated Ps (black, dotted) and the population in ground (blue, dashed) and excited (red, dash-dotted) states (right axis) at t = 120 ns. The green line in –o– style gives the value of n_r (scaled by a factor of 5 for visibility) at the end of the laser-Ps interaction. Bottom: Plot of the time evolution of the 1D-temperature T_z and populations in the usual state categories for the three magnetic field strengths 0, 0.3, and 1 T. The green lines indicate the time evolution of n_r(ON)/N (–o– style), n_r(OFF)/N (–x– style), and $S = [n_r(\text{ON})\text{-}n_r(\text{OFF})]/n_r(\text{OFF})$ (with triangles), all scaled by a factor of 5. Same color code as in Fig. 3. A cloud of $N = 2000$ atoms and standard laser parameters have been used.

field cases. Indeed, since the triplet and singlet states are not mixed by any external electromagnetic field, no enhancement of the annihilation happens during the excitation process. At $t = 120$ ns, the 1D temperature has dropped below 50 K and the number of slow atoms has increased by more than a factor of 3.

The situation is quite different for the low B-field regime. For $B = 0.3$ T, the annihilation is enhanced during the whole cooling interaction, which is consistent with the Zeeman effect mixing short- and long-living states. A third of the initial population of the Ps cloud is initialized in the $m = 0$ ground state (mainly triplet one), that is, coupled to the (mainly singlet) $m = 0$ ground state (short lifetime). These atoms quickly annihilate and are responsible for the fast increase of the annihilation at the beginning of the simulation. As the strength of the magnetic field increases, the mixing between triplet and singlet $m = 0$ ground states becomes stronger, increasing the speed and the total amount of annihilation of Ps at the end of the laser interaction. As shown in the upper part of Fig. 5, once the Paschen-Back regime is reached for $n = 2$ ($B \gtrapprox 1$ T), the total amount of annihilation at $t = 120$ ns does not vary with the magnetic field any longer.

Indeed, for $B = 1$ T and higher values of the magnetic field, a similar sudden initial annihilation jump is observed. In the same way as for lower values of B, this jump corresponds to the annihilation of the atoms initially in $m = 0$ (mainly) triplet state, Zeeman coupled to the $m = 0$ singlet state, and lasts until about 10 ns. At this point, all atoms initially in the $m = 0$ triplet state are annihilated. As a result, the annihilation rate is much slower and comparable to what is observed for $B = 0$ T. This is due to the decoupling between m_l and m_S states for the $n = 2$ levels. In this strong B-field regime, the laser interaction starting on $m = \pm 1$ ground states (which annihilate slowly), mainly keeps cycling on long-living states, decoupled from short-living states.

As shown in Fig. 2, in the Paschen-Back regime, three state branches have developed due to the Zeeman effect. With the appropriately detuned laser, cooling becomes much more efficient again. From these results we conclude that, even though the laser-Ps interaction increases the number of slow atoms (n_r) for all values of the magnetic field, if possible, laser cooling experiments should be carried out either in magnetic fields of $B \lesssim 0.05$ T or environments of fairly high field strengths above 1 T to ensure laser interaction with high efficiency.

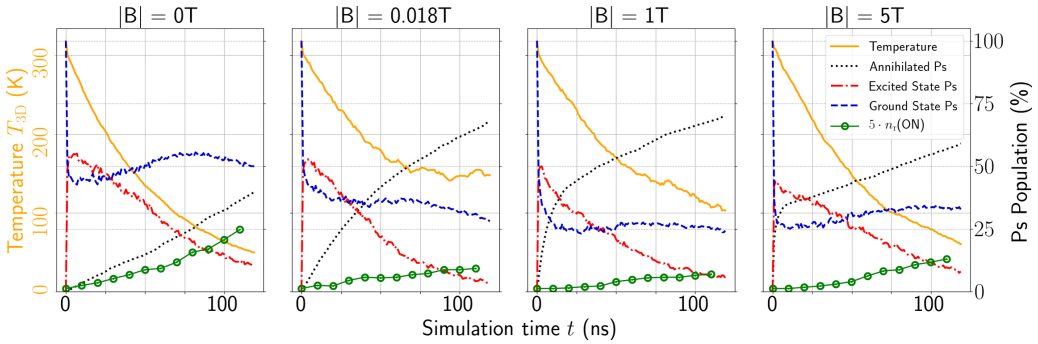

FIG. 6. 3D cooling. Left axis: Evolution of T_{3D} (orange, solid line). Right axis: Evolution of the fraction of annihilated Ps atoms (black, dotted), the fraction of Ps atoms in the $n = 1$ ground state (blue, dashed) and the $n = 2$ excited state (red, dash-dotted), normalized by N (the initial number of atoms) for four different magnetic field strengths 0, 0.018, 1, and 5 T. The green line in -o— style represents $n_r^{(3D)}(\mathrm{ON})/N$, scaled by a factor of 5. The plots are based on the results of simulations for a cloud of 2000 Ps atoms initialized at 300 K and isotropically expanding in all three spatial directions in a static magnetic field $\boldsymbol{B}$. The cloud is cooled by three pairs of left-/right-circularly polarized counterpropagating beams along x, y, and z, each beam with a power of 2 kW, 75 GHz bandwidth and detuned by $-2.5\,\mathrm{cm}^{-1}$.

VII. 2D AND 3D CASES

We now consider 2D and 3D Ps laser cooling, starting with a 3D configuration with lasers irradiating a 3D isotropically expanding Ps cloud from all three spatial directions, for different magnetic field strengths and draw general conclusions on the feasibility of 3D laser cooling.

The 3D expanding cloud is in all cases initialized at a temperature of 300 K and the counterpropagating laser beams always have the standard left-/right-circular polarization. Each beam has a 2 kW power. As the main figure of merit for 3D cooling, we use the effective 3D temperature T_{3D}, which is the rms value of the three individual 1D temperatures T_x, T_y, and T_z. For 2D cooling, we use the 2D temperature T_{2D}, which is the rms value of the two individual 1D temperatures T_x and T_y. We also introduce $n_r^{(3D)}(\mathrm{ON})$ defined as the number of atoms with velocity $\sqrt{v_x^2 + v_y^2 + v_z^2} \leqslant 16 \times v_r$ for 3D cooling and $n_r^{(2D)}(\mathrm{ON})$ defined as the number of atoms with velocity $\sqrt{v_x^2 + v_y^2} \leqslant 8 \times v_r$ for 2D cooling. The coefficients 16 and 8 in the definition of $n_r^{(3D)}(\mathrm{ON})$ and $n_r^{(2D)}(\mathrm{ON})$ are arbitrary and were chosen to ensure that enough atoms contribute to the calculation of n_r in each case.

A. Laser cooling in 3D

To investigate the influence of the magnetic field on the 3D-cooling performance, we simulate laser cooling of the Ps cloud for four values of the B field (0, 0.018, 1, and 5 T) in the previously identified favorable regions. Figure 6 gives an overview of the corresponding results.

All laser beams have the same standard optimized set of parameters as for 1D cooling.

The population in the excited state quickly becomes nearly equal to or slightly higher than the population in the ground state for all values of the magnetic field which confirms that the saturation regime is reached. As in the previous 1D studies, we notice the same fast enhanced annihilation process for the nonzero magnetic field cases. Indeed, shortly after $t \approx 1$ ns, half of the initial number of Ps atoms is in the excited state for $B = 0$ T and only a third of N is excited for $B = 5$ T. This is consistent with fast annihilation of the $m = 0$ triplet ground state in a strong magnetic field due to the Zeeman effect. In all cases, the population in the ground state stays almost constant over time. This means that spontaneous emission from the excited states tends to compensate the losses due to annihilation and reexcitation. As a result, the population in the excited states decreases at the same rate as annihilation in the ground state increases. For $B = 0$ T, the annihilation rate is lower during 3D cooling compared to 1D cooling, which is consistent with the idea that the average lifetime of Ps increases when more atoms are excited to $n = 2$ (infinite lifetime for the excited states compared to $n = 1$ levels). As mentioned in Sec. III, this is valid only given that the excitation does not populate mixed states that could decay toward the $n = 1$, $m = 0$ states with shorter lifetimes. In the zero-magnetic field case, this is ensured all the time because the laser interaction occurs only between triplet states. $B = 0.018$ T is an intermediate situation where the $m = 0$ triplet ground state does not annihilate instantaneously at $t = 0$ ns but still annihilates faster than the $m = \pm 1$ states which breaks the *stationary* regime observed for the other values of magnetic field presented in Fig. 6.

In the opposite, and as also seen in the 1D case studies, for high field regimes, the decoupling of m_s and m_l allows one to separate three branches of states (see Fig. 2). However, this regime is reached for higher magnetic fields in $n = 1$ compared to the excited level. Therefore, the ground $m = 0$ states (triplet-singlet superposition) are still mixed even for 5 T, and a fast initial annihilation of all the atoms in the $m = 0$ ground state is observed during the first few ns. After this initial (almost) instantaneous annihilation of the atoms in the $m = 0$ ground state, the annihilation rate becomes smaller again, consistent with the $B = 0$ T annihilation rate of the atoms in the $m = \pm 1$ ground states. We also observe that the total amount of annihilated atoms is higher in the 0.018 and 1 T cases compared to the 5 T one. By selecting the proper detuning of the laser, one can cycle only on long-living states, avoiding the states mixed by the Zeeman effect that would decay toward the $m = 0$ ground states. The Zeeman effect at 1 T and higher is strong enough to reach the Paschen-Back regime for the $n = 2$ states, where three branches of states of different lifetimes are split in energy (see Fig. 2). The further

away these branches are in energy, the easier it is to tune the laser frequency such that the resonant transitions excite only long-living states. Therefore, the 5 T case seems to be more favorable than the other intermediate field strengths' configuration. We observe in Fig. 6 that both T_{3D} and $n_r^{(3D)}(ON)$ have better values for $B = 0$ T and 5 T than for the intermediate values of magnetic field.

For these two extreme cases, the final temperature of the cloud can reach below 100 K and the number of slow atoms ($n_r^{(3D)}$) can increase by at least a factor of 6 in 0 T and by a factor of 2 in 5 T, for a 100 ns laser interaction time. In contrast, for the experimentally more typical values of magnetic field 0.018 T and for 1 T [42–44], the temperature can merely be reduced down to 150 K.

Finally, a comparison between T_z for 1D longitudinal cooling and T_{3D} suggests that 3D- cooling is less efficient than 1D cooling in both 0 T and 5 T. While temperatures of almost 40 K can be reached for 1D longitudinal cooling in 5 T, the minimal 3D temperature merely drops below 100 K. This is simply due to the fact that in 3D, three times more events are required to scatter the same amount of photons per axis as in 1D. By varying the laser parameters in our simulations for optimization, we found that for best cooling results in terms of final 3D temperature, it is advisable to choose the same bandwidth and detuning values as in 1D. As far as the laser power is concerned, slightly higher values than in 1D are recommended. To summarize these studies, when choosing an external environment, it is preferable to ensure performing 3D laser cooling either in a zero-magnetic field region or in a high magnetic field region to reach the Paschen-Back regime for $n = 2$.

B. 2D and 3D beam experiments

In this section, we report on studies of experimental setups with Ps atoms emitted by a positron converter target. The first application focuses on the case of 2D transverse cooling with the objective of creating a collimated beam by reducing the angular spread of the expanding cloud. In the second application, a moving molasses is cooled transversely while keeping a distinct mean velocity.

For these two applications, the Ps ensemble is modeled as an effusive beam formed after positron implantation into a nanochannelled silicon Ps-reflection target [4]. Once thermalized inside the target, the Ps has a 3D isotropic Maxwellian distribution $f(v) = (\frac{m}{2\pi k_B T})^{3/2} 4\pi v^2 e^{-\frac{mv^2}{2k_B T}}$. Thus, during the time interval dt, the number of Ps atoms ejected from the target under an angle θ with respect to the normal of the target, that is, in the conical solid angle $d\Omega = \sin(\theta) d\theta d\phi$ (in spherical coordinates) and with a velocity $\|\boldsymbol{v}\|$ between v and $v + dv$, is proportional to $f(v) v \cos(\theta) dt d\Omega dv$. We create such a distribution by means of the inverse transform sampling (Smirnov inverse probability integral transform). In real experiments, the thermalization and ejection process produce a time spread of about ten nanoseconds. However, for simplicity, here we model the effusive beam as an area of $(0.1 \times 2 \times 2)\,\text{mm}^3$ representing the typical 2 mm spot which Ps atoms are emitted from. Thus, creating all Ps atoms at time $t = 0$ but in a spatial slab of 0.1 mm parallel to the target mimics the proper time distribution.

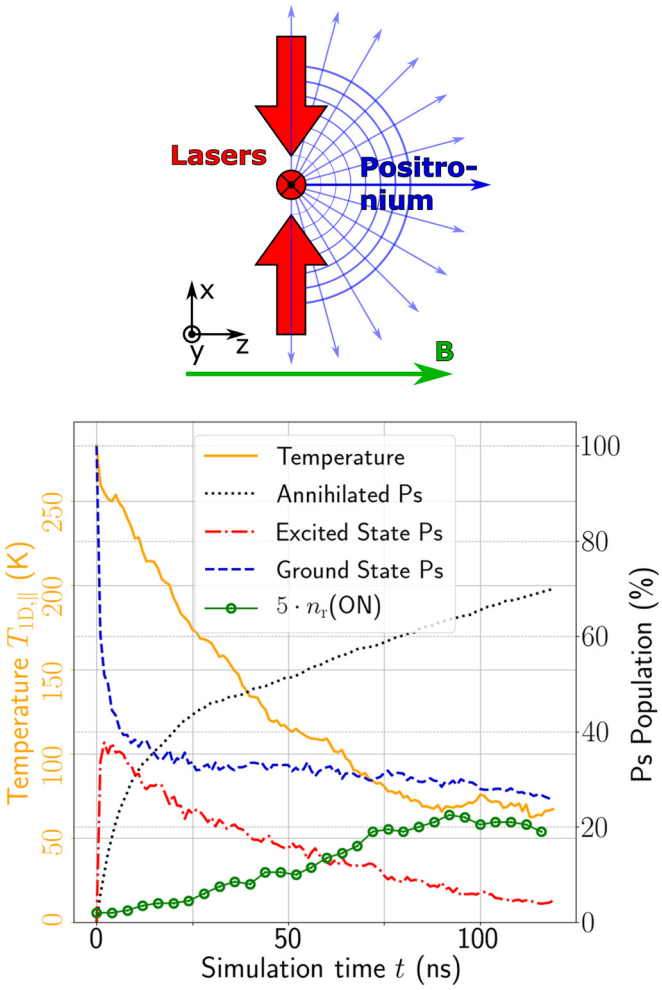

FIG. 7. 2D transverse cooling in 1 T. The sketch on the left illustrates the experimental setup including the magnetic field $\boldsymbol{B}$ (green arrow) along z, two pairs of counterpropagating laser beams along x and y (red arrows), and Ps emission (blue) as an effusive beam along z originating from a 2 mm spot. The plot on the right shows the time evolution of the populations, T_{2D} and $n_r^{(2D)}(ON)/N$. Same color code as in Fig. 3.

To quantify the cooling process of a beam, which is intrinsically a phase space density enhancement, we use the (4D) reduced beam brightness B_r, that is the total current I (here number of Ps per second emitted by the target) divided by the beam area, by the solid angle divergence and by the beam kinetic energy $\frac{1}{2}mv_z^2$. So $B_r = \frac{I}{8\pi^2 \sigma_x \sigma_y k_B \sqrt{T_x T_y}}$, where σ_x and σ_y are the rms width of the beam in the x and y direction, respectively [45]. B_r is an invariant along the beam path for any Hamiltonian force field and, thus, only true cooling (neither filtering nor slowing) can increase it [35,45–48].

Consistently with the definition of the temperature parameter, we take into account only the particles from the second and third quartiles of the distribution to evaluate σ_x and σ_y in the calculation of B_r.

1. 2D transverse cooling in 1 T

Here, 2D laser cooling of the effusive beam in a field of 1 T aligned parallel to the Ps propagation direction z is reported.

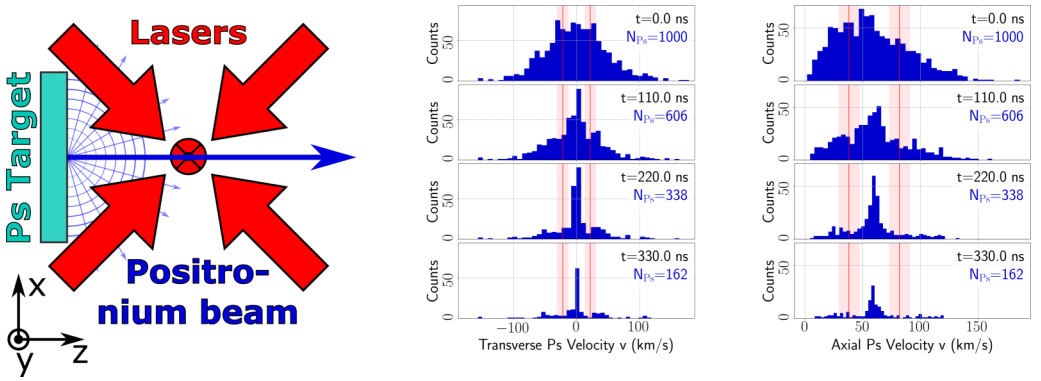

FIG. 8. 3D moving molasses cooling in zero field. As shown in the sketch on the left, six crossed laser beams from all spatial directions, with the ones in the (x-z)-plane being tilted by 45°, address the effusive Ps beam generated by a reflective Ps formation target offset by 8 mm with respect to the laser crossing point. The evolution of the transverse (respectively axial) velocity component distribution is presented in the middle (respectively, right) panels.

The laser configuration consists of two pairs of counterpropagating beams in the transverse (x-y) plane with standard circular polarization. The main goal of such an experiment is to reduce the solid angle of the Ps beam by means of laser cooling. We found cooling to be optimized again for similar laser parameters as for 1D cooling.

The sketch on the left in Fig. 7 illustrates the setup. The results of the simulation are plotted on the right part of the figure, featuring the evolution of the temperature parameter T_{2D} (the rms value of T_x and T_y) and the population in selected state categories.

Compared to 3D cooling in 1 T, there are about 5% less atoms in excited states and the annihilation curves are almost identical, which is consistent with a negligible decrease of the average lifetime of the Ps atoms due to this 5% difference in the excited state population.

The results validate a successful collimation of the Ps beam thanks to 2D transverse laser cooling. T_{2D} can be reduced down to 70 K and $n_r^{(2D)}(\mathrm{ON})$ is multiplied by a factor of 10 over the course of 120 ns. Finally, the brightness is increased by a factor of 7 at $t = 120$ ns.

2. 3D moving molasses

Finally, we report on 3D cooling of the effusive Ps beam, emitted by a reflective positron converter target, in kind of a moving molasses configuration as sketched in Fig. 8. The goal is to control the three components of the velocity to produce a monochromatic beam that can be sent to another experimental chamber for interferometric measurements, for instance. Therefore, these studies are carried out in an environment with very low (negligible but nonzero to impose a quantization axis) magnetic field. In real experiments, such small fields would result in a large positron implantation area, typically on the order of 2 mm.

In addition to the reduction of the transverse angular spread, this scheme aims at focusing the distribution along the propagation direction z to a well-defined mean velocity v_{mean}.

In this setup, to prevent damage to the target, the lasers are not sent directly onto it. Thus, to accommodate a target of 2 mm length, it is offset by 8 mm along the z axis (see Fig. 8) while keeping all laser beams aligned onto the origin. The previous configuration of two transverse pairs of counterpropagating laser beams is replaced by a set of three pairs of counterpropagating laser beams. One pair is still lying purely in the transverse plane (pointing along y) while the other two form a cross in the (x-z) plane, which also contains the Ps propagation direction. These two beams are tilted by 45° with respect to the Ps beam. We chose $v_{\mathrm{mean}} = 60\,\mathrm{km/s}$ as the target mean velocity, well in the range of the thermal velocity distribution at 300 K. Thus, for each pair of counterpropagating beams in the (x-z) plane, the detuning values of the two counterpropagating beams have to differ by $\pm\frac{1}{\sqrt{2}}\frac{v_{\mathrm{mean}}}{c}E_0 = \pm 5.82\,\mathrm{cm}^{-1}$ from resonance (E_0), in addition to the detuning δ required for 3D cooling.

Figure 8 shows the evolution of the distributions of velocity components both in transverse (middle panel) and axial direction (right panel) at four equidistant time steps. Because it takes almost 130 ns for the emitted Ps to reach the crossing point with the laser beams, we simulate the evolution of the cooling process for the time span of 330 ns during which the lasers are constantly on and shining light along the three spatial directions.

The process efficiency is highest for the same bandwidth of 75 GHz coinciding with the width of the Doppler distribution. However, as far as the detuning and the power are concerned, the results differ from all previous settings. Instead of $\delta = -2.5\,\mathrm{cm}^{-1}$ and $P = 2\,\mathrm{kW}$, the atoms are collimated best around the target mean velocity for the slightly higher values of $-3.0\,\mathrm{cm}^{-1}$ and 5 kW.

The distributions of both the transverse and axial velocity components confirm that the two goals of this application can be reached. The width of the initial distribution in the transverse direction and thus the velocity dispersion is clearly reduced during the 330 ns of laser-Ps interaction, implying an efficient collimation of the Ps cloud along the direction of propagation of interest (longitudinal axis). This is also reflected by the final transverse 2D temperature, which is the rms value of T_x and T_y, $T_{2D} = 10.5\,\mathrm{K}$.

In the axial direction, the width of the distribution is narrowed and centered around the desired velocity of 60 km/s. The rather high cooling efficiency compared to the previous application is, to a large extent, due to the fact that this 3D cooling of the effusive beam in the moving molasses scheme is

carried out in an almost zero-field environment. This implies that the level structure is influenced neither by Zeeman nor motional Stark effects.

VIII. CONCLUSION

We studied laser cooling in the presence of a magnetic field in several configurations. For magnetic field values between 0.05 T and 0.7 T, laser cooling is predicted to show low efficiency and annihilation is strongly enhanced. Indeed, in this range of magnetic field, the Ps atoms quickly annihilate due to Zeeman mixing both in the ground and the excited states, the number of slow atoms remains low, and only few cycles of absorption/emission can be done before annihilation.

However, 1D, 2D, and 3D laser cooling outside this range of magnetic field seems promising even though losses are usually higher than in zero field. During the ∼120 ns cooling time, it is possible to reduce velocities by more than few tens of km/s. One way to further reduce the final velocity could be to proceed with a frequency sweep using a relatively narrow laser bandwidth. The cooling could start with a far detuned laser to cool the faster atoms and the resonance frequency would be tuned down as long as the atoms get cooler and cooler. However, for Ps atoms, this method should be carefully thought out because annihilation limits the possible total time of laser cooling. The capture range of the laser interaction should not be chosen too small even in the case of a sweep detuning in order not to slow down the process too much, as we discussed in the 1D dynamical studies.

We also proposed realistic 2D- and 3D-cooling schemes, for example, as a tool to reduce the solid angle of a Ps beam. The final temperature clearly depends on the initial velocity distribution of the Ps atoms. The final values of temperature reached in our simulations are typically below 50 K when starting at 300 K to simulate, for instance, the thermalized fraction of Ps emitted by a room-temperature nanoporous silicon target. However, the recoil temperature can be reached by 1D cooling of a Ps cloud with ∼10 K initial temperature (such as produced by charge exchange [49]). It is, in principle, even possible to reach temperatures below the Ps recoil temperature of 0.15 K using laser spectrum shaping [14].

One possible application of this study, which would highly benefit from such a collimated beam, is the production of antihydrogen by means of charge exchange between Rydberg Ps and antiprotons [50,51]. According to our numerical studies, for a cooling time of 120 ns, the brightness of the beam can be enhanced typically by a factor of 7. As a second example, we reported on 3D cooling of a Ps moving molasses. Such a resulting monokinetic beam with well-defined axial mean velocity and better collimation due to reduced angular spread could subsequently be used for time of flight or optical grating experiments as well as interferometry [3,4].

Finally, such high-density cold Ps also paves the way to the production of a Ps BEC which would open up the possibility for many great applications such as the realization of a gamma ray laser [52] or studies on antimatter gravity. For this type of study, the code should be extended to include multiple scattering effects between positronium atoms and account for processes such as the formation of Ps_2 molecules [53], light-induced collisions, or photon rescattering producing a repulsive force, for example. The study presented here is expected to be valid only for densities of positronium lower than $10^{12}\,\mathrm{cm}^{-3}$.

ACKNOWLEDGMENTS

We acknowledge the members of the AEgIS (Antihydrogen Experiment: Gravity, Interferometry, Spectroscopy) collaboration for fruitful discussions. This work was supported by the Research Council of Norway under Grant Agreement No. 303337 and by Domaine d'Intérêt Majeur Science et Ingénierie en Région Île-de-France pour les Technologies Quantiques (DIM SIRTEQ) grant LASANTI. LASANTI grant from the PME 2020 call of the DIM (in French: Domaine d'intérêt majeur) SIRTEQ (in French: SCIENCE ET INGNIERIE EN RÉGION ÎLE-DE-FRANCE POUR LES TECHNOLOGIES QUANTIQUES) and from the IQUPS project (in French: Ingénierie Quantique à l'Université Paris-Saclay) which is an "Initiative de Recherche stratégique" of the Université Paris-Saclay.

APPENDIX A: POSITRONIUM PROPERTIES

For completeness, and to avoid misprints or different phase conventions in angular momentum coupling present in the literature (see, for instance, Refs. [2,29–31,54,55]), we find it useful to recall here some basic formulas to calculate positronium properties.

1. Atomic units

We will sometimes use atomic units but adapt them to the Ps reduced mass: $\mu = \mu(Ps) = m_e/2$ compared to the infinite nucleus mass $\mu(\infty) = m_e$ for the standard atomic units or to $\mu(H) = m_e m_p/(m_e + m_p)$ for the hydrogen atom. m_e is the electron mass and m_p the proton one. Distances are expressed in terms of the (Bohr) radius $a_0^{(\mu)} = \frac{4\pi\epsilon_0\hbar^2}{\mu e^2}$, energies by means of the (Hartree) energy $E_h^{(\mu)} = \frac{e^2}{4\pi\epsilon_0 a_0^{(\mu)}}$, the electric field in $E_{au}^{(\mu)} = \frac{E_h^{(\mu)}}{e a_0^{(\mu)}}$, and the magnetic field in $B_{au}^{(\mu)} = \frac{\hbar}{e(a_0^{(\mu)})^2}$. For Ps, this results in $a_0 = a_0^{(Ps)} = 2a_0^{\mu(\infty)} = 1.05836 \times 10^{-10}\,\mathrm{m}$, $E_h = E_h^{(Ps)} = E_h^{\mu(\infty)}/2 = 2.17987 \times 10^{-18}\,\mathrm{J}$, $E_{au} = E_{au}^{(Ps)} = E_{au}^{\mu(\infty)}/4 = 1.28555 \times 10^{11}\,\mathrm{V/m}$, $B_{au} = B_{au}^{(Ps)} = B_{au}^{\mu(\infty)}/4 = 58762.7\,\mathrm{T}$.

a. Energy levels

We use the formulas given by Ref. [2] corrected by an (obvious) misprint,

$$E/E_h = -\frac{1}{2n^2} + \frac{2\alpha^2}{n^3}\left[\frac{11}{64n} - \frac{1+\epsilon/2}{2(2l+1)}\right], \qquad \text{(A1)}$$

where $\epsilon = 0$ for singlet ($S = 0$) states. For triplet states ($S = 1$) $\epsilon = -\frac{7}{3}$ for $S, l = 0$ states and $\epsilon = \delta_{j,l+1}\frac{-(3l+4)}{(l+1)(2l+3)} + \delta_{j,l}\frac{1}{l(l+1)} + \delta_{j,l-1}\frac{3l-1}{l(2l-1)}$ for all others. More elaborate formulas exist (see, for instance, Ref. [56]) but they are not required for the accuracy needed for this paper.

b. Annihilation lifetime

Based of Refs. [2,57–59] (with a correction between GHz and s^{-1}), we use for the annihilation rates:

$$\begin{aligned}
\Gamma^{\rm ann}(n^1{\rm S}_0) &= \frac{n^{-3}}{125.1\,{\rm ps}} \approx n^{-3}\frac{\alpha^5}{2}\frac{m_e c^2}{\hbar},\\
\Gamma^{\rm ann}(n\,^3{\rm S}_1) &= \frac{n^{-3}}{142.0\,{\rm ns}} \approx n^{-3}\frac{2(\pi^2-9)\alpha^6}{9\pi}\frac{m_e c^2}{\hbar},\\
\Gamma^{\rm ann}(n\,^3{\rm P}_2) &= \frac{n^2-1}{30n^5}\alpha^7\frac{m_e c^2}{\hbar},\\
\Gamma^{\rm ann}(n\,^3{\rm P}_1) &= 0,\\
\Gamma^{\rm ann}(n\,^3{\rm P}_0) &= \frac{n^2-1}{8n^5}\alpha^7\frac{m_e c^2}{\hbar},\\
\Gamma^{\rm ann}(n\,^1{\rm P}_1) &= \frac{n^2-1}{9\pi n^5}\ln\left(\frac{8n^2}{\alpha^2}\right)\alpha^8\frac{m_e c^2}{\hbar}.
\end{aligned} \tag{A2}$$

We assume negligible annihilation times for higher l states.

2. Dipole matrix element

a. Reduced dipole matrix element

The dipole $\boldsymbol{d} = e\boldsymbol{r}$ matrix elements between $|nlm\rangle$ and $|n'l'm'\rangle$ states are given by

$$\begin{aligned}
\langle n'l'm'|r_q/a_0|nlm\rangle &= C^{l'm'}_{lm,1q}\frac{\langle n'l'\|r/a_0\|nl\rangle}{\sqrt{2l'+1}}\\
&= C^{l'm'}_{lm,1q}C^{l'0}_{l0,10}\frac{\sqrt{2l+1}}{\sqrt{2l'+1}}R^{n'l'}_{nl},
\end{aligned} \tag{A3}$$

where q is the polarization component (in more detail below) and $C^{jm}_{j_1m_1,j_2m_2}$ is the Clebsch-Gordan with Condon-Shortley phase convention [60]. The overlap $R^{n'l'}_{nl}$ is directly the atomic unit value:

$$\begin{aligned}
R^{n'l-1}_{nl} &= \frac{(-1)^{n'-l}}{4(2l-1)!}\sqrt{\frac{(l+n)!(l+n'-1)!}{(-l+n-1)!(n'-l)!}}\frac{(4nn')^{l+1}(n-n')^{n+n'-2l-2}}{(n+n')^{n+n'}}\\
&\times\left({}_2F_1\left(l-n+1,l-n',2l,-\frac{4nn'}{(n-n')^2}\right)-\frac{(n-n')^2}{(n'+n)^2}\,{}_2F_1\left(l-n-1,l-n',2l,-\frac{4nn'}{(n-n')^2}\right)\right).
\end{aligned} \tag{A4}$$

b. Photoionization cross section

We calculate the photoionization rate

$$\Gamma^{\rm pi}_{ji} = \sum_{\rm L}\frac{I_{\rm L}}{\hbar\omega_{\rm L}}\sigma_i^j$$

from a state i to a continuum state j, by lasers of intensity $I_{\rm L}$ and photon energy $\hbar\omega_{\rm L}$, by using the cross section σ_i^j.

For the continuum level of energy $E > 0$, it is convenient to define k, in a corresponding way to the binding energy $-\frac{E_h}{2n^2}$ of level n, as $E = \frac{E_h}{2}k^2$. Thus, the link is $n = i/k$. The photoionization cross section from state $|nlm\rangle$ to state $|k'l'm'\rangle$ is given by

$$\sigma^{k'l'm'}_{nlm} = 4\pi^2\alpha a_0^2\left(\frac{1}{n^2}+k'^2\right)|\langle k'l'm'|r_{(m'-m)}/a_0|nlm\rangle|^2,$$

where $R^{k'l'}_{nl}$, for $l' = l+1$ and $l' = l-1$, is given by

$$\begin{aligned}
R^{k'l+1}_{nl} &= \frac{-i}{4k'(2l+1)!}\sqrt{\frac{1}{2}\frac{(n+l)!\prod_{s=1}^{l+1}(1+s^2k'^2)}{(n-l-1)!(1-e^{-\frac{2\pi}{k'}})}}\left(\frac{4n}{1+n^2k'^2}\right)^{l+2}e^{-\frac{2}{k'}\arctan(nk')}\left(\frac{n-i/k'}{n+i/k'}\right)^{n-l-2}\\
&\times\left({}_2F_1\left(l+2-i/k',l+1-n;2l+2;-\frac{4n\,i/k'}{(n-i/k')^2}\right)-\left(\frac{n-i/k'}{n+i/k'}\right)^2{}_2F_1\left(l-i/k',l+1-n;2l+2;-\frac{4ni/k'}{(n-i/k')^2}\right)\right),
\end{aligned} \tag{A5}$$

$$\begin{aligned}
R^{k'l-1}_{nl} &= \frac{-1}{4(2l+1)!}\sqrt{\frac{1}{2}\frac{(n+l)!\prod_{s=1}^{l-1}(1+s^2k'^2)}{(n-l-1)!(1-e^{-\frac{2\pi}{k'}})}}\left(\frac{4n}{1+n^2k'^2}\right)^{l+1}e^{-\frac{2}{k'}\arctan(nk')}\left(\frac{n-i/k'}{n+i/k'}\right)^{n-l-1}\\
&\times\left({}_2F_1\left(l-i/k',l+1-n;2l;-\frac{4n\,i/k'}{(n-i/k')^2}\right)-\left(\frac{n-i/k'}{n+i/k'}\right)^2{}_2F_1\left(l-i/k',l-1-n;2l;-\frac{4ni/k'}{(n-i/k')^2}\right)\right).
\end{aligned} \tag{A6}$$

3. Stark and Zeeman effect

Using these units, the Hamiltonian for Ps at velocity v (but also for hydrogen or the protonium atom, except for the Zeeman term (cf. Appendix of Ref. [55]) is given by $H = H_0 + H_{\rm S} + H_{\rm Z}$, where (in atomic units) $H_0 = -\frac{1}{2}\frac{\partial^2}{\partial r^2} - \frac{1}{r}$ is the atomic

Hamiltonian, $H_S = \boldsymbol{r}\cdot(\boldsymbol{E}+\boldsymbol{v}\times\boldsymbol{B})$ the Stark Hamiltonian and $H_Z = -\frac{1}{8}(\boldsymbol{r}\times\boldsymbol{B})^2 + \frac{1}{4}g_e\boldsymbol{B}\cdot(\boldsymbol{S}_{e^+}-\boldsymbol{S}_{e^-})$ the Zeeman one with $g_e \approx -2.002319$. The matrix element has to be expressed in the fine structure basis $|nlsjm\rangle$.

a. Stark effect and dipole transitions

The Stark effect, or according dipole transitions, are described by (cf., for instance, [60], p. 381)

$$\langle n'l's'j'm'|r_q/a_0|nlsjm\rangle = \delta_{s's}(-1)^{j+l'+s-1}\sqrt{2j+1}C^{j'm'}_{jm,1q}\begin{Bmatrix} l & s & j \\ j' & 1 & l' \end{Bmatrix}C^{l'0}_{l0,10}\sqrt{2l+1}R^{n'l'}_{nl}. \tag{A7}$$

Exactly the same formula is valid for transitions towards the continuum after replacing n' by k'.

We have chosen to couple $\boldsymbol{l}+\boldsymbol{s}=\boldsymbol{j}$ instead of $\boldsymbol{s}+\boldsymbol{l}=\boldsymbol{j}$. This choice is crucial to be consistent for the Stark, Zeeman and dipole transition formulas because $\boldsymbol{l}+\boldsymbol{s}=\boldsymbol{j}$ or $\boldsymbol{s}+\boldsymbol{l}=\boldsymbol{j}$ lead to different phases that can in turn result in wrong and inconsistent results after diagonalization of the full Hamiltonian.

b. Zeeman effect

For the Zeeman effect, we neglect the quadratic term that plays an important role only for Rydberg states (the formula can be found in Ref. [61]). Switching from the reduced units to International System of Units (SI, from the French name "Système international"), the linear Zeeman effect thus becomes $\hat{H}_Z|m_{e^-}m_{e^+}\rangle = (-g_e)\mu_B B(m_{e^-}-m_{e^+})|m_{e^-}m_{e^+}\rangle$ or $\hat{H}_Z|s,m_s\rangle = (-g_e)\mu_B B\delta_{0m_s}|1-s,0\rangle$, where $\mu_B = \frac{e\hbar}{2m_e}$ is the Bohr magneton. The standard coupling $\boldsymbol{l}+\boldsymbol{s}=\boldsymbol{j}$ then immediately leads to

$$\langle n'l's'j'm'|H_Z|nlsjm\rangle = (-g_e)\mu_B B\delta_{n'n}\delta_{l'l}\delta_{s,1-s'}\delta_{m'm}C^{jm}_{lm,s0}C^{j'm'}_{l'm',s'0}. \tag{A8}$$

APPENDIX B: SIMULATION CODE

The program, which has partially been described in Ref. [38] and is accessible at Ref. [39] solves the rate equations for absorption and for spontaneous and stimulated emission. It simulates (shaped) laser excitation and motion under external forces and, for charged particles, takes into account N-body Coulombian interactions and Lorentz forces.

The system is supposed to evolve under classical forces (dipolar + magnetic + electric + gravity) and the scattering force is implemented by means of the momentum recoil in absorption and stimulated or spontaneous emission steps.

One key assumption of the code is that in the absence of photon absorption or emission, the system has an adiabatic evolution. In our Ps case, the external magnetic field $\boldsymbol{B}$ defines the $|nlsjm\rangle$ state with respect to the quantization axis (with momentum projection m) represented by $\boldsymbol{B}$, so the state is labeled as $|nlsjm\rangle_{\boldsymbol{B}}$. Due to adiabaticity and in the absence of photon effects which can lead to state changes, the state remains in $|nlsjm\rangle_{\boldsymbol{B}(t)}$ while moving under the field $\boldsymbol{B}$ at any time t.

The dynamical Stark effect adds complexity to the system because the levels are mixed in $\boldsymbol{E}$ and $\boldsymbol{B}$ fields, so care has to be taken to properly follow the states during diagonalization of the Hamiltonian. In the case of absorption or spontaneous emission events, the velocity changes due to the accompanying recoil so the dynamical Stark effect changes as well, which in turn might lead to altered level ordering. We have verified that this is not the case in the $n=1$ manifold so the random recoil for the spontaneous emission can be safely calculated using an ordered level scheme.

The light shift is implemented but not applied since it is negligible for our purpose of laser cooling and its calculation slows down the code.

We recall here that the code calculates the time for an internal state change (all rate equations for light interaction) and compares it to the external state evolution (time step fixed at 500 ps in our case). The evolution is then solved by means of a KMC algorithm and an N-body (Verlet) solver as discussed in Ref. [38].

As detailed in the next section, the stimulated emission and absorption rate for a transition $i \leftrightarrow j$ for a laser with polarization vector $\boldsymbol{\epsilon}$ is given by

$$\gamma = \gamma_{ij} = \frac{\pi(\boldsymbol{d}\cdot\boldsymbol{\epsilon})^2[I_\omega \otimes L](\omega+\boldsymbol{k}\cdot\boldsymbol{v}-\omega_{ij})}{\hbar^2\epsilon_0 c} \tag{B1}$$

(correcting the missing factor $\hbar^2$ in Formula (B.7) in Ref. [38]). The transition has a spontaneous emission rate of

$$\Gamma_{ij} = \frac{\omega^3}{3\pi\varepsilon_0\hbar c^3}|\boldsymbol{d}_{ij}|^2, \tag{B2}$$

where $\boldsymbol{d}_{ij} = e\langle i|\boldsymbol{r}|j\rangle$ is the transition dipole moment. We also use the notation $\Gamma_{i\leftarrow j}$ for the spontaneous emission rate from state $|j\rangle$ to state $|i\rangle$, which occurs only if $E_j > E_i$. As a result, $\Gamma_{i\leftarrow j} = \Gamma_{ij}$ if $E_j > E_i$ and $\Gamma_{i\leftarrow j} = 0$ if $E_i > E_j$.

The local intensity results from the convolution of the laser spectrum I_ω with the Lorentzian transition line shape $L(\delta) = \frac{\Gamma_{ij}}{2\pi}\frac{1}{(\Gamma_{ij}/2)^2+\delta^2}$, where $\delta = \omega-\omega_{ij}$ denotes the detuning and $I_\omega(\omega)$ the laser's spectral irradiance distribution (throughout the paper, we improperly use the word intensity). With the full laser irradiance $I = \int I_\omega(\omega)d\omega$, the electric field of the laser becomes $E = \sqrt{2I/\epsilon_0 c}$). In our case, the lasers have a Gaussian spectrum which leads to a Voigt profile for the transition rate γ_{ij}, which we approximate as given in Ref. [62].

For a laser with a Lorentzian spectrum with FWHM Γ_L, the rate simplifies to $\gamma = I\frac{\pi(\boldsymbol{d}.\boldsymbol{\epsilon})^2}{\hbar^2\epsilon_0 c}\frac{\Gamma_{ij}+\Gamma_L}{2\pi}\frac{1}{((\Gamma_{ij}+\Gamma_L)/2)^2+\delta^2}$ with the Doppler induced detuning $\delta = \omega+\boldsymbol{k}\cdot\boldsymbol{v}-\omega_{ij}$. This formula helps us understand how bound-bound and bound-free rates can be treated in a similar manner. While on resonance $\gamma = \frac{\Omega_{ij}^2}{\Gamma_{ij}+\Gamma_L} = 4\pi^2\alpha\frac{d_{ij}^2}{e^2}\frac{2I}{\hbar(\Gamma_{ij}+\Gamma_L)}$, photoionization is described by $\gamma = 4\pi^2\alpha\frac{d_{ij}^2}{e^2}\frac{2I}{E_h}$. Thus photoionization can be considered as a bound-bound transition with a linewidth given by the Rydberg constant $E_h/2$.

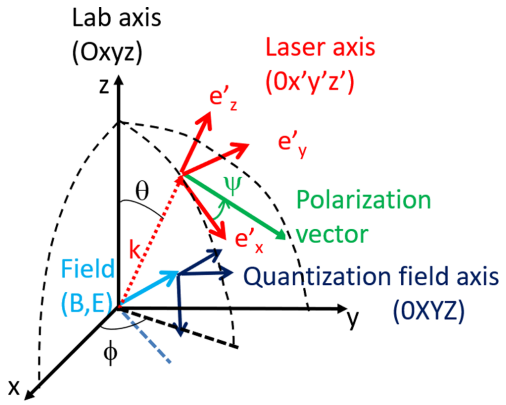

FIG. 9. Definition of the different frames: Laser axis (for the polarization basis), field axis (which is the quantization axis since we assume adiabatic following of the states), and fixed laboratory frame. To switch from the fixed laboratory frame to the laser axis, we perform a first rotation by an angle ϕ around the z axis followed by a second rotation by an angle θ around the new y axis.

APPENDIX C: DETAILS OF LASER INTERACTION

The laser interaction is already partly described in Ref. [38], the quantization, recoil, and Doppler effects in Ref. [35] (Supplemental Material) and vector and angular momenta in Refs. [60,63]. We want to recall here some important points while using less assumptions (especially concerning the reality of some vectors). We have thus accordingly modified the notations given in Ref. [38].

1. Spherical and helicity vectors

For the (covariant) spherical vectors, we use the same notations as in Ref. [60], such as $\mathbf{e}_0 = \mathbf{e}_z$ and $\mathbf{e}_{\pm 1} = \mp(\mathbf{e}_x \pm i\mathbf{e}_y)/\sqrt{2}$. Using $\mathbf{e}^q = (\mathbf{e}_q)^* = (-1)^q \mathbf{e}_{-q}$ (which leads to the normalization $\mathbf{e}^p \mathbf{e}_q = \delta_{pq}$), we find for any (complex) vector

$$\boldsymbol{A} = \sum_q A^q \mathbf{e}_q = \sum_q (-1)^q A_{-q} \mathbf{e}_q,$$

where $A_q = \boldsymbol{A} \cdot \mathbf{e}_q$ with, for instance, $A_0 = A_z$ and $A_{\pm 1} = \mp(A_x \pm iA_y)/\sqrt{2}$. It is often the case that A_q or A^q are real numbers (for example, some dipoles with pure laser polarization) but, in general, we should keep in mind that the vectors are complex.

2. Lasers using complex notations

The electromagnetic field $\boldsymbol{E}(\boldsymbol{r}, t) = \boldsymbol{E}'(\hat{\boldsymbol{r}}, t) + \boldsymbol{E}'^{\dagger}(\hat{\boldsymbol{r}}, t)$ of the lasers (L), can be written as

$$\boldsymbol{E}(\boldsymbol{r}, t) = \frac{1}{2} \sum_{\mathrm{L}} [\boldsymbol{E}_{\mathrm{L}} e^{i(\boldsymbol{k}_{\mathrm{L}} \cdot \boldsymbol{r} - \Phi_{\mathrm{L}}(t))} + \boldsymbol{E}_{\mathrm{L}}^* e^{-i(\boldsymbol{k}_{\mathrm{L}} \cdot \boldsymbol{r} - \Phi_{\mathrm{L}}(t))}],$$

where $I_{\mathrm{L}} = \varepsilon_0 |E_{\mathrm{L}}|^2 c/2$ is the irradiance, improperly called intensity.

The Doppler effect and the laser linewidth are taken into account by writing $\Phi_{\mathrm{L}}(t) = (\omega_{\mathrm{L}} - \boldsymbol{k}_{\mathrm{L}} \cdot \boldsymbol{v}) \times t + \Phi^{\mathrm{L}}(t)$ with the fluctuating phase $\Phi^{\mathrm{L}}(t)$.

As shown in Fig. 9, for describing the laser we use the (covariant polar basis) frame linked to the laser propagation ($\mathbf{e}'_{\mathrm{x}} = \mathbf{e}_\theta, \mathbf{e}'_{\mathrm{y}} = \mathbf{e}_\phi, \mathbf{e}'_{\mathrm{z}} = \mathbf{e}'_{\mathrm{r}} = \boldsymbol{k}_{\mathrm{L}}/\|\boldsymbol{k}_{\mathrm{L}}\|$). The laser polarization is conveniently described in the (covariant) helicity basis by $\mathbf{e}'_0 = \mathbf{e}'_z$, $\mathbf{e}'_{\pm 1} = \mp(\mathbf{e}'_x \pm i\mathbf{e}'_y)/\sqrt{2}$. For each laser L, the polarization vector, defined as $\boldsymbol{E}_{\mathrm{L}}(\boldsymbol{r}, t) = E_{\mathrm{L}}(\boldsymbol{r}, t)\boldsymbol{\epsilon}_{\mathrm{L}}$, is given by $\boldsymbol{\epsilon}_{\mathrm{L}} = \sum_{p=-1,0,+1} \epsilon'^p \mathbf{e}'_p$ with $E_{\mathrm{L}} \geqslant 0$.

3. Transition dipole moment

The transition dipole moment (we often use the simplified notation $\boldsymbol{d} = e\boldsymbol{r}$ known from the simple cases of H, Ps, or alkali atoms) between two levels is (for the moment in the fixed laboratory frame which will be explained in Appendix C 5 b) defined as $\boldsymbol{d}_{ij} = \langle i|\boldsymbol{d}|j\rangle = \sum_q (-1)^q d_{ij;q} \mathbf{e}_q = \sum_q d_{ij;q} \mathbf{e}^q$, so $d_{ij;q} = \boldsymbol{d}_{ij} . \mathbf{e}_q$. Often the notation $d_{ij}^{(q)} = d_{ij;q}$ is used but this should be avoided due to possible confusion with the (contravariant) notation d_{ij}^q. The correct components forming an irreducible tensor (rank 1) $\hat{d}_{1q} = \hat{d}_q$ are $d_{ij;-1}, d_{ij;0}, d_{ij;+1}$. In general, the dipoles are complex, but often, such as in field-free cases or in those with well-defined quantization axis with the proper (Condon-Shortley's type) convention [60], they can be real.

4. Absorption, stimulated, or spontaneous emission

For a transition between two states $|j\rangle$ to $|i\rangle$, it is important to distinguish between absorption (rising level energy) and stimulated or spontaneous emission (lowering level energy) since this decides on the term to be used in the rotating wave approximation.

In the following, we assume $E_j > E_i$.

a. Ordered energy levels and rotating wave approximation

For level j above level i (i.e., $E_j > E_i$), the rotating wave approximation leads to

$$\hat{H} = \frac{\hat{\boldsymbol{p}}^2}{2m} + V_i(\hat{\boldsymbol{r}}, t)|i\rangle\langle i| + V_j(\hat{\boldsymbol{r}}, t)|j\rangle\langle j| - \langle j|q\hat{\boldsymbol{r}}|i\rangle \cdot \boldsymbol{E}'(\hat{\boldsymbol{r}}, t)|j\rangle\langle i| - \langle i|q\hat{\boldsymbol{r}}|j\rangle \cdot \boldsymbol{E}'^{\dagger}(\hat{\boldsymbol{r}}, t)|i\rangle\langle j|, \tag{C1}$$

where potentials V_i and V_j have been added to be more general.

In the code, the states $|i, \boldsymbol{p}\rangle$ are defined by their internal state i and momentum $\boldsymbol{p}$. The fields are treated in a classical way where the recoil effect is present, only after interaction takes place, by means of a $\hbar\boldsymbol{k}$ term added to the momentum: $e^{\pm i\boldsymbol{k}\cdot\hat{\boldsymbol{r}}}|\boldsymbol{p}\rangle = |\boldsymbol{p} \pm \hbar\boldsymbol{k}\rangle$.

b. Absorption, stimulated, or spontaneous emission

Absorption is thus a transition $i \to j$ ($E_j > E_i$). For absorption, the only relevant term in the Hamiltonian is $-\boldsymbol{d} \cdot \boldsymbol{E}'$ determined by the Rabi frequency $\Omega_{j \leftarrow i} = \Omega_{ji}$ [64]:

$$\hbar\Omega_{ji} = E_{\mathrm{L}}\langle j, \boldsymbol{p} + \hbar\boldsymbol{k}|\hat{\boldsymbol{d}} \cdot \boldsymbol{\epsilon}_{\mathrm{L}} e^{i\boldsymbol{k}\cdot\hat{\boldsymbol{r}}}|i, \boldsymbol{p}\rangle = E_{\mathrm{L}} \boldsymbol{d}_{ji} \cdot \boldsymbol{\epsilon}_{\mathrm{L}} = E_{\mathrm{L}} \sum_q d_{ji;q} \mathbf{e}^q . \sum_p \epsilon'^p \mathbf{e}'_p \tag{C2}$$

On the other hand, stimulated emission $j \to i$ provoked by the same laser is governed by the $-\boldsymbol{d}.\boldsymbol{E}'^{\dagger}$ term and thus arises from the Rabi frequency $\hbar\Omega_{ij} = E_{\mathrm{L}}\langle i, \boldsymbol{p} - \hbar\boldsymbol{k}|\hat{\boldsymbol{d}}.\boldsymbol{\epsilon}_{\mathrm{L}}{}^{\dagger} e^{-i\boldsymbol{k}.\hat{\boldsymbol{r}}}|j, \boldsymbol{p}\rangle = E_{\mathrm{L}} \boldsymbol{d}_{ij}.\boldsymbol{\epsilon}_{\mathrm{L}}{}^{\dagger} = \hbar\Omega_{ji}^*$.

The dipole transition rates are the similar (conjugated Rabi frequencies) for spontaneous and stimulated emission.

The simplest (ideal) case is given if

(1) The quantization and laser axes (used for the polarization) are equal $\mathbf{e}_q = \mathbf{e}'_q$. In this case, the absorption is driven by $\hbar\Omega_{ji} = E_\mathrm{L}\sum_q d_{ji;q}\epsilon'^q$.

(2) The laser has pure polarization, i.e., $\epsilon'^q = 1$ for a given q and 0 for others so $\hbar\Omega_{ji} = E_\mathrm{L} d_{ji;q}$.

(3) States are pure (that means with well-defined magnetic quantum numbers m_i, m_j as the projection on the quantization axis $\mathbf{e}_0$). So $\hbar\Omega_{ji} = E_\mathrm{L} d_{ji;q} = E_\mathrm{L}\langle j|d_{1q}|i\rangle$ is nonzero only if $m_j = q + m_i$ so $q = -1$ for a $\sigma-$, $q = 0$ for a π, and $q = +1$ for a $\sigma+$ laser.

In the following, we will treat the most general case where none of these three assumptions is correct.

5. Rotation matrices

As illustrated in Fig. 9, we have to consider three frames:

(1) The fixed laboratory frame $(\mathbf{e}_\mathrm{x}, \mathbf{e}_\mathrm{y}, \mathbf{e}_\mathrm{z})$.

(2) The local (different for each particle position $\boldsymbol{r}$) field $\boldsymbol{F}(\boldsymbol{r})$ frame, $(\mathbf{e}_\mathrm{X}, \mathbf{e}_\mathrm{Y}, \mathbf{e}_\mathrm{Z})$ which defines the quantization axis. It will also be written as $(\mathbf{E}_\mathrm{X}, \mathbf{E}_\mathrm{Y}, \mathbf{E}_\mathrm{Z} = \mathbf{F}/\|\mathbf{F}\|)$ to define the vectors $\mathbf{E}_{\pm1}$ to avoid confusion with $\mathbf{e}_{\pm1}$.

(3) The laser frame $(\mathbf{e}'_\mathrm{x}, \mathbf{e}'_\mathrm{y}, \mathbf{e}'_\mathrm{z} = \mathbf{k}/\|\mathbf{k}\|)$.

These frames are defined by their respective z, z', Z axis and by the convention for the angle of rotation around this axis as defined in Fig. 9. The laser z' frame, for example, is the polar frame where Oz' is the direction and Ox' is the meridian.

a. Euler angles

Euler angles are applied to change from one $(\mathbf{e}_\mathrm{x}, \mathbf{e}_\mathrm{y}, \mathbf{e}_\mathrm{z})$ frame to a new one $(\mathbf{e}'_\mathrm{x}, \mathbf{e}'_\mathrm{y}, \mathbf{e}'_\mathrm{z})$. Different conventions exist: MATHEMATICA and [60] (1.4 schema A) use the so-called z y z (also written as Z Y Z) convention, whereas Ref. [65] is based on the z x z convention. For completeness, we thus recall here the convention for the Euler rotation angles (α, β, γ). In the z y z convention, for instance:

(1) The first rotation is by an angle α about the z axis.

(2) The second rotation is by an angle β around the new y axis.

(3) Finally, the third rotation is by an angle γ with respect to the new z axis (now z').

As shown in Fig. 9, our convention based on the spherical basis leads to $(\alpha, \beta, \gamma) = (\phi, \theta, 0)$ in the z y z convention but $(\alpha, \beta, \gamma) = (\phi + \pi/2, \theta, -\pi/2)$ in the z x z convention.

For historical reasons, the z x z convention is used in the code. This convention is useful to find the polar angles ϕ, θ only based on the vector $\mathbf{e}'_z = x_e\mathbf{e}_\mathrm{x} + y_e\mathbf{e}_\mathrm{y} + z_e\mathbf{e}_\mathrm{z}$, which defines the new frame: $\alpha = \phi + \pi/2 = \mathrm{atan2}(x_e, -y_e)$ and $\beta = \theta = \arccos(z_e)$. Since the calculation of the function atan2 is extremely slow, we use approximations which can be found in Refs. [66–68].

Using simple notations such as $s_\alpha = \sin(\alpha)$ or $c_\gamma = \cos(\gamma)$, the new coordinates are given by

$$\begin{pmatrix} x \\ y \\ z \end{pmatrix} = \begin{pmatrix} c_\alpha c_\gamma - c_\beta s_\alpha s_\gamma & -c_\alpha s_\gamma - c_\beta c_\gamma s_\alpha & s_\alpha s_\beta \\ c_\gamma s_\alpha + c_\alpha c_\beta s_\gamma & c_\alpha c_\beta c_\gamma - s_\alpha s_\gamma & -c_\alpha s_\beta \\ s_\beta s_\gamma & c_\gamma s_\beta & c_\beta \end{pmatrix} \begin{pmatrix} x' \\ y' \\ z \end{pmatrix}.$$

This matrix (or the inverse one) is, for instance, used to find the laser intensity at the particle location $\boldsymbol{r} = x\mathbf{e}_\mathrm{x} + y\mathbf{e}_\mathrm{y} + z\mathbf{e}_\mathrm{z}$.

b. Polarization vectors

To evaluate Eq. (C2), the laser polarization vector is written in the three frames using vector notations $\boldsymbol{\epsilon}_\mathrm{L} = \sum_p \epsilon'^p \mathbf{e}'_p = \sum_p \mathcal{E}^p \mathbf{E}_p = \sum_p \epsilon^p \mathbf{e}_p$. This can be written as $\boldsymbol{\epsilon}_\mathrm{L} = \boldsymbol{e}'_\cdot \boldsymbol{\epsilon}'^\cdot = \mathbf{E}_\cdot \boldsymbol{\mathcal{E}}^\cdot = \mathbf{e}_\cdot \boldsymbol{\epsilon}^\cdot$ by means of

$$\boldsymbol{\epsilon}'^\cdot = \begin{pmatrix} \epsilon'^{-1} \\ \epsilon'^{0} \\ \epsilon'^{+1} \end{pmatrix} = \begin{pmatrix} a_- \, e^{i\Psi} \\ 0 \\ a_+ \, e^{-i\Psi} \end{pmatrix}$$

for the laser polarization vector (which has no component along its propagation axis),

$$\boldsymbol{e}'_\cdot = (\mathbf{e}'_{-1}\, \mathbf{e}'_0\, \mathbf{e}'_{+1}), \quad \boldsymbol{\mathcal{E}}^\cdot = \begin{pmatrix} \mathcal{E}^{-1} \\ \mathcal{E}^0 \\ \mathcal{E}^{+1} \end{pmatrix}, \quad \boldsymbol{E}_\cdot = (\mathbf{E}_{-1}\, \mathbf{E}_0\, \mathbf{E}_{+1}),$$

$$\boldsymbol{\epsilon}^\cdot = \begin{pmatrix} \epsilon^{-1} \\ \epsilon^{0} \\ \epsilon^{+1} \end{pmatrix},$$

and $\boldsymbol{e}_\cdot = (\mathbf{e}_{-1}\, \mathbf{e}_0\, \mathbf{e}_{+1})$.

Next, we call $\phi_{\boldsymbol{k}}, \theta_{\boldsymbol{k}}$ the polar angles of $\boldsymbol{k}$ (to go from the fixed laboratory frame to the laser frame) and $\phi_{\boldsymbol{F}}, \theta_{\boldsymbol{F}}$ the polar angles of $\boldsymbol{F}$ (to go from the laboratory frame to the field frame). Equation 1.1 (53) from Ref. [60] then gives $\sum_p \mathbf{e}_p d^1_{pp'}(\phi_{\boldsymbol{k}}, \theta_{\boldsymbol{k}}, 0) = \mathbf{e}'_{p'}$ which is $\mathbf{e}_\cdot \boldsymbol{D}(\phi_{\boldsymbol{k}}, \theta_{\boldsymbol{k}}, 0) = \mathbf{e}'_\cdot$ and, similarly, $\mathbf{e}_\cdot \boldsymbol{D}(\phi_{\boldsymbol{F}}, \theta_{\boldsymbol{F}}, 0) = \mathbf{E}_\cdot$, where $(\boldsymbol{D})_{ij} = d^1_{ij}$ is the WignerD function.

Here again several conventions exist: MATHEMATICA WignerD $[\{j, m_1, m_2\}, \alpha, \beta, \gamma]$ which is equal to $d^j_{m_1,m_2}(-\alpha, -\beta, -\gamma)$ in Ref. [60]. We use the latter one which is also the one chosen in Ref. [69] with

$$\boldsymbol{D}(\phi, \theta, 0) = \begin{pmatrix} \frac{1}{2}e^{i\phi}(1+\cos\theta) & \frac{e^{i\phi}\sin\theta}{\sqrt{2}} & e^{i\phi}\sin^2(\theta/2) \\ -\frac{\sin\theta}{\sqrt{2}} & \cos\theta & \frac{\sin\theta}{\sqrt{2}} \\ e^{-i\phi}\sin^2(\theta/2) & -\frac{e^{-i\phi}\sin\theta}{\sqrt{2}} & \frac{1}{2}e^{-i\phi}(1+\cos\theta) \end{pmatrix},$$

with the order $i, j = -1, 0, 1$ for the lines and columns.

Because states $|i\rangle$ are defined with respect to the quantization axis frame $\mathbf{E}_\cdot$, we note $\boldsymbol{d}_{ij} = \langle i|\boldsymbol{d}|j\rangle = \sum_q D_{ij;q}\mathbf{E}^q$ with $D_{ij;q} = \boldsymbol{d}_{ij}.\mathbf{E}_q$. In matrix notation, with $\boldsymbol{D}_{ij\cdot} = (D_{ij;-1}\, D_{ij;0}\, D_{ij;+1}) = (D_{-1}\, D_0\, D_{+1})$ and

$$\boldsymbol{E}^\cdot = \begin{pmatrix} \mathbf{E}^{-1} \\ \mathbf{E}^0 \\ \mathbf{E}^{+1} \end{pmatrix},$$

this results in $\boldsymbol{d}_{ij} = \boldsymbol{D}_{ij\cdot}\mathbf{E}^\cdot$

We finally write Eq. (C2) as

$$\hbar\Omega_{ij}/E_\mathrm{L} = \boldsymbol{d}_{ij}\cdot\boldsymbol{\epsilon}_\mathrm{L} = [\boldsymbol{D}_{ij\cdot}\mathbf{E}^\cdot]\cdot[\boldsymbol{e}'_\cdot\boldsymbol{\epsilon}'^\cdot] = \boldsymbol{D}_{ij\cdot}\boldsymbol{D}^{-1}(\phi_{\boldsymbol{F}}, \theta_{\boldsymbol{F}}, 0)\boldsymbol{D}(\phi_{\boldsymbol{k}}, \theta_{\boldsymbol{k}}, 0)\begin{pmatrix} a_- \, e^{i\Psi} \\ 0 \\ a_+ \, e^{-i\Psi} \end{pmatrix}. \quad \text{(C3)}$$

Thus, the final result is

$$\begin{aligned}\hbar\Omega_{ij}/E_{\mathrm{L}} = &\frac{1}{4}e^{-i(\psi+\phi_F+\phi_k)}\\ &\times[\cos(\theta_k)(-a_+ + a_- e^{2i\psi})((e^{2i\phi_F}+e^{2i\phi_k})(\sqrt{2}D_0\sin(\theta_F)+(D_- - D_+)\cos(\theta_F)) - (D_- + D_+)(e^{2i\phi_F}-e^{2i\phi_k}))\\ &- 2\sin(\theta_k)e^{i(\phi_F+\phi_k)}(-a_+ + a_- e^{2i\psi})(\sqrt{2}D_0\cos(\theta_F)+(D_+ - D_-)\sin(\theta_F))\\ &+(a_+ + a_- e^{2i\psi})((D_- + D_+)(e^{2i\phi_F}+e^{2i\phi_k}) - (e^{2i\phi_F}-e^{2i\phi_k})(\sqrt{2}D_0\sin(\theta_F)+(D_- - D_+)\cos(\theta_F)))]\end{aligned}$$

6. Stark effect

The Stark effect $\hat{H}_{\mathrm{Stark}} = -\hat{\boldsymbol{d}}.\boldsymbol{E}$ caused by an external electric field $\boldsymbol{E}$ is given by the exact same Hamiltonian as the dipolar transition. The calculation is thus very similar, providing that now the polarization vector (field orientation) is, in fact, along the field (along $\boldsymbol{k}$), so

$$\boldsymbol{\epsilon} = \begin{pmatrix}\epsilon^{-1}=0\\ \epsilon^{0}=1\\ \epsilon^{+1}=0\end{pmatrix}.$$

The final result is

$$\begin{aligned}\langle i|\hat{\boldsymbol{d}}.\boldsymbol{E}|j\rangle = &\frac{1}{2}[\cos(\theta_k)(2D_0\cos(\theta_F)+\sqrt{2}(D_+ - D_-)\sin(\theta_F))\\ &+\sin(\theta_k)(\sqrt{2}(D_- - D_+)\cos(\theta_F)\cos(\phi_F-\phi_k)+2D_0\cos(\phi_F-\phi_k)\sin(\theta_F) - i\sqrt{2}(D_- + D_+)\sin(\phi_F-\phi_k))].\end{aligned} \tag{C4}$$

7. Angular distribution of spontaneous emission: recoil

To correctly take into account the recoil momentum, it is essential to know the angular distribution of the emitted photon. For that, we have to go back to the calculation of the spontaneous emission rate that originates from the quantized field (where $\boldsymbol{\epsilon}_{k\pm1} = \mathbf{e}'_{\pm1}$), i.e., from (Fermi's golden rule) $\sum_{k,\pm1}|\langle i|\boldsymbol{d}|j\rangle\cdot\boldsymbol{\epsilon}_{k\pm1}|^2 = \sum_k[\sum_p|\boldsymbol{d}_{ji}\cdot\boldsymbol{e}'_{kp}|^2 - |\boldsymbol{d}_{ji}\cdot\boldsymbol{e}'_{k0}|^2]$. By defining the polarization vector of the emitted light as $\mathbf{e}_{\mathrm{pol}} = \boldsymbol{d}_{ji}/\|\boldsymbol{d}_{ji}\|$, we find that the probability distribution for the direction $\boldsymbol{r} = \boldsymbol{k}/k$ of the emitted photon is given by

$$\frac{3}{8\pi}[1-|\boldsymbol{r}\cdot\mathbf{e}_{\mathrm{pol}}|^2] \tag{C5}$$

with the proper normalization. In the code, the photon is taken from this distribution, calculated using the Von Neumann's acceptance-rejection sampling method.

8. Diagonalization of the states

In most cases, the eigenstates themselves do not change during the evolution, only the energy changes. However, the Hamiltonian needs to be diagonalized, for instance, to calculate Zeeman and Stark effects by the magnetic $\boldsymbol{B}$ and, if required, electric $\boldsymbol{E}$ fields more exactly. For this purpose, the bare states $|i\rangle_0$, their energies E_{i0}, and the dipole transition moments are expressed by means of three matrices $\{\boldsymbol{d}0_{-1}, \boldsymbol{d}0_0, \boldsymbol{d}0_{+1}\}$ in the quantization frame (always assuming adiabatic following), where $(\boldsymbol{d}0_q)_{ij} = d0_{ij;q} = {}_0\langle i|\hat{\boldsymbol{d}}|j\rangle_0\cdot\mathbf{E}_q$.

For each local (Stark+Zeeman) perturbation $\hat{V}(\boldsymbol{B}(\boldsymbol{r}),\boldsymbol{E}(\boldsymbol{r}))$, the Hamiltonian $\hat{H} = \hat{H}_0 + \hat{V}$ is then diagonalized to obtain the new eigenvectors $|i\rangle = \sum_{i_0}{}_0\langle i_0|i\rangle|i_0\rangle_0 = \sum_{i_0}\mathcal{V}_{i_0 i}|i_0\rangle_0$ with the eigenvector matrix $\mathcal{V}_{i_0 i} = {}_0\langle i_0|i\rangle$. From this, the new dipoles $\langle i|\hat{d}_q|j\rangle = (\mathcal{V}^\dagger\cdot\boldsymbol{d}0_q\cdot\mathcal{V})_{ij}$ are calculated which are coded by the (complex) dipole vector $\{d_{ij;-1}, d_{ij;0}, d_{ij;+1}\}$.

APPENDIX D: RATE EQUATIONS, KINETIC MONTE CARLO, AND *N*-BODY INTEGRATOR

1. Rates

The rate equations used in our simulation for any level $|i\rangle$ with population P_{i} are given by

$$\begin{aligned}\dot{P}_j &= -\left(\Gamma_j^{\mathrm{ann}}+\Gamma_j^{\mathrm{pi}}\right)P_{\mathrm{j}} + \sum_i \gamma_{ji}P_{\mathrm{i}} - (\Gamma_{i\leftarrow j}+\gamma_{\mathrm{ij}})P_{\mathrm{j}},\\ \dot{P}_i &= -\left(\Gamma_i^{\mathrm{ann}}+\Gamma_i^{\mathrm{pi}}\right)P_{\mathrm{i}} + \sum_j(\Gamma_{i\leftarrow j}+\gamma_{\mathrm{ij}})P_{\mathrm{j}} - \gamma_{\mathrm{ji}}P_{\mathrm{i}},\end{aligned} \tag{D1}$$

where we assume $E_j > E_i$.

The absorption and stimulated emission rate γ_{ij} is calculated using Eq. (B1), where, for every laser L, the Rabi frequency Ω_{ij}^{L} characterizes the strength of the transition between the states $|i\rangle$ and $|j\rangle$ occurring with the detuning

$$\delta_{ji}^{\mathrm{L}} = \omega_{\mathrm{L}} - \omega_{ji} - \boldsymbol{k}_{\mathrm{L}}\cdot\boldsymbol{v}.$$

Although the code can implement interferences between lasers, as explained in Ref. [38], we do not use it here since we assume incoherent (mainly broadband multimode) lasers.

The spontaneous emission rate Γ_{ij} is calculated using Eq. (B2) with the dipole $\boldsymbol{d}_{ij}$ given by the coherent superposi-

tion of the eigenstates (not the incoherent sum as erroneously done in Ref. [31]).

To treat annhiliation and photoionization in a similar way as spontaneous and stimulated emission, in our code we add extra dead and continuum levels j_0, toward which the annihilation or photoionization rates in zero field are calculated as, respectively, a spontaneous emission rate and an absorption one.

The annihilation rate of state $|i\rangle$ [calculated using Eq. (A2)] becomes

$$\Gamma_i^{\text{ann}} = \sum_{i_0} |\mathcal{V}_{i_0 i}|^2 \Gamma_{i_0}^{\text{ann}}. \tag{D2}$$

In the code, it is convenient to treat $\Gamma_{i_0}^{\text{ann}}$ as a spontaneous emission rate toward a dead level j_0. For this reason, we create five such $n = 0$ states, with $m = -2, -1, 0, 1, 2$, with (arbitrary) energies $-10000\,\text{cm}^{-1}$ below the $n = 1$ manifold and with a dipole transition such that the rate, calculated as a spontaneous emission rate, is the annihilation rate: $\Gamma_{i_0}^{\text{ann}} = \Gamma_{j_0 \leftarrow i_0}$

The photoionization in the presence of magnetic and electric fields is a very complex process with quantization of the cyclotron frequency, Landau resonance, etc. We therefore simplify the system and treat this loss channel similarly as annihilation. We thus assume it to be an incoherent sum over unperturbated levels:

$$\Gamma_{ji}^{\text{pi}} = \sum_{i_0} \left|\mathcal{V}_{i_0 i}\right|^2 \Gamma_{ji_0}^{\text{pi}}.$$

This is an average treatment that underestimated cases with constructive interference and overestimated cases with destructive interferences.

Similarly, it is convenient to treat $\Gamma_{ji_0}^{\text{pi}} = \Gamma_{j_0 i_0}^{\text{pi}}$ as a stimulated emission rate toward a continuum level j_0 (since being unaffected by Zeeman and Stark effects, $j_0 = j$ applies, as for the dead levels). Therefore, we create seven such states $n = \infty$, with $m = -3, -2, -1, 0, 1, 2, 3$, located at the ionization threshold energy with a dipole transition such that the rate, calculated as a stimulated rate, is the photoionization rate (for the 243 nm laser): $\Gamma_{j_0 i_0}^{\text{pi}} = \gamma_{j_0 i_0}$.

2. Kinetic Monte Carlo to solve rate equations

A KMC algorithm is used to solve the rate equations by choosing the optimal time step evolution of the system. The KMC method is indistinguishable from the behavior of the real system, reproducing, for instance, all possible data in an experiment including statistical noise.

The KMC algorithm is implemented in the following steps:

(1) Initialization of the system to its given state called k at the actual time t.

(2) Creation of the new rate list γ_{lk} for the system, $l = 1, \ldots, N$.

(3) Choosing a unit-interval uniform random number generator [70] r: $0 < r \leqslant 1$ and calculating the first reaction rate time t' by solving $\int_t^{t'} \sum_{l=1}^{N} \gamma_{lk}(\tau) d\tau = -\ln r$.

(4) Choosing a unit-interval uniform random number generator r': $0 < r' \leqslant 1$ and searching for the integer l for which $R_{l-1} < r' R_N \leqslant R_l$ where $R_j = \sum_{i=1,j} \gamma_{ik}(t')$ and $R_0 = 0$. This is done efficiently using a binary search algorithm.

(5) Setting the system to state l and modifying the time to t'. Finally, going back to the first step.

3. Equations of motion

We use here a simple but still efficient algorithm, the so-called velocity leapfrog-Verlet-Störmer-Delambre algorithm:

$$\begin{aligned} \mathbf{r}(t + \Delta t) &= \mathbf{r}(t) + \mathbf{v}(t)\Delta t + \tfrac{1}{2}\mathbf{a}(t)(\Delta t)^2, \\ \mathbf{v}(t + \Delta t) &= \mathbf{v}(t) + \tfrac{1}{2}(\mathbf{a}(t) + \mathbf{a}(t + \Delta t))(\Delta t). \end{aligned} \tag{D3}$$

It has an accuracy of $O((\Delta t)^3)$ for both position $\mathbf{r}$ and velocity $\mathbf{v}$ for a Δt time step. This algorithm has the big advantage that the accuracy can be improved by using higher order symplectic integrators.

In our case, the velocity is modified directly by photon recoils caused by absorption or emission events and the acceleration is simply calculated using the gradient of the potential. A typical timescale is given by the atom's motion in the laser (or, if existing, inhomogeneous external) fields. Thus, the time step should be a small fraction of the ratio between laser waist (or the typical inhomogeneity size) and the particle's thermal velocity to ensure energy conservation at all times.

Finally, the KMC and the N-body integrator are combined in the following way: we first calculate an expected (KMC) reaction time $t' - t$. Then, if $t' - t < \Delta t$, that means a reaction occurs prior to the full motion, the particles are moved according to Eq. (D3) using the time step $t' - t$, and the reaction takes place at time t'. On the contrary, if $\Delta t < t' - t$, the system evolves dynamically (N body) without any reaction taking place but, due to its Markovian probabilistic behavior, it is still governed by Eq. (D1). Next, after each change of position or internal state, the laser fields and potentials are recalculated and new transition rates are calculated. It is convenient to choose a Δt time step such that the calculated laser excitation rates are almost constant over Δt to allow calculation of the reaction time $t' - t = -\frac{\ln r}{\sum_{l=1}^{N} \Gamma_{lk}(t)}$. We use these rules of thumb to start the simulation but we finally reduce the time step Δt until we obtain convergence of the results which usually occurs for $\gamma \Delta t \sim 1$.

[1] M. Charlton, A. Mills Jr, and Y. Yamazaki, Special issue on antihydrogen and positronium, J. Phys. B: At., Mol. Opt. Phys. **50**, 140201 (2017).

[2] D. Cassidy, Experimental progress in positronium laser physics, Eur. Phys. J. D **72**, 53 (2018).

[3] M. Oberthaler, Anti-matter wave interferometry with positronium, Nucl. Instrum. Methods Phys. Res. B **192**, 129 (2002).

[4] S. Mariazzi, R. Caravita, M. Doser, G. Nebbia, and R. Brusa, Toward inertial sensing with a $2\,^3$S positronium beam, Eur. Phys. J. D **74**, 1 (2020).

[5] A. Mills, Jr. and M. Leventhal, Can we measure the gravitational free fall of cold Rydberg state positronium? Nucl. Instrum. Methods Phys. Res., Sec. B **192**, 102 (2002).

[6] P. Platzman and A. Mills Jr, Possibilities for Bose condensation of positronium, Phys. Rev. B **49**, 454 (1994).

[7] S. Adhikari, Positronium interaction and its Bose-Einstein condensation, Phys. Status Solidi C **6**, 2272 (2009).

[8] T. Hirose, T. Asonuma, H. Iijima, M. Irako, K. Kadoya, T. Kumita, B. Matsumoto, N. Mondal, K. Wada, H. Yabu *et al.*, Laser cooling of ortho-positronium: Toward realization of Bose-Einstein condensation, in *Quantum Aspects of Beam Physics* (World Scientific, 2002), pp. 279-282.

[9] K. Shu, X. Fan, T. Yamazaki, T. Namba, S. Asai, K. Yoshioka, and M. Kuwata-Gonokami, Study on cooling of positronium for Bose Einstein condensation, J. Phys. B **49**, 104001 (2016).

[10] A. Ishida, S. Kenji, M. Tomoyuki, F. Xing, N. Toshio, A. Shoji, Y. Kosuke, K. Makoto, O. Nagayasu, E. Brian *et al.*, Study on positronium Bose-Einstein condensation, in *JJAP Conference Proceedings* (The Japan Society of Applied Physics, 2017), Vol. 7.

[11] K. Shu, T. Murayoshi, X. Fan, A. Ishida, T. Yamazaki, T. Namba, S. Asai, K. Yoshioka, M. Kuwata-Gonokami, N. Oshima *et al.*, Study on Bose-Einstein condensation of positronium, in *Journal of Physics: Conference Series* (IOP Publishing, Matsue, Japan, 2017), Vol. 791, p. 012007.

[12] A. Mills, Jr., Positronium Bose-Einstein condensation in liquid He4 bubbles, Phys. Rev. A **100**, 063615 (2019).

[13] N. Mondal, Challenges and advances of positronium Bose-Einstein condensation, AIP Adv. **9**, 055310 (2019).

[14] Edison P. Liang and Charles D. Dermer, Laser cooling of positronium, Opt. Commun. **65**, 419 (1988).

[15] D. Cassidy, H. Tom, and A. Mills Jr, Fundamental physics with cold positronium, AIP Conference Proceedings **1037**, 66 (2008).

[16] C. Hugenschmidt, International school of physics qe. fermi course clxxiv: Physics with many positrons, *Proceedings of the International School of Physics "Enrico Fermi", Course CLXXIV: Physics with many positrons*, Vol. 174 (IOS Press, 2010), pp. 399–417.

[17] P. Crivelli, D. Cooke, and S. Friedreich, Experimental considerations for testing antimatter antigravity using positronium 1s-2s spectroscopy, in *International Journal of Modern Physics: Conference Series* (World Scientific, 2014), Vol. 30, p. 1460257.

[18] H. Iijima, T. Asonuma, T. Hirose, M. Irako, T. Kumita, M. Kajita, K. Matsuzawa, and K. Wada, Laser cooling system of ortho-positronium, Nucl. Instru. Meth. Phys. Res. A **455**, 104 (2000).

[19] N. N. Mondal, Construction of a position-sensitive scintillation detectors system to view the laser cooled ortho-positronium, in *Nuclear Science Symposium Conference Record, 2001 IEEE* (IEEE, 2001), Vol. 1, pp. 319–324.

[20] T. Kumita, T. Hirose, M. Irako, K. Kadoya, B. Matsumoto, K. Wada, N. Mondal, H. Yabu, K. Kobayashi, and M. Kajita, Study on laser cooling of ortho-positronium, Nucl. Instru. Meth. Phys. Res. B **192**, 171 (2002).

[21] K. Wada, T. Asonuma, T. Hirose, H. Iijima, M. Irako, K. Kadoya, T. Kumita, B. Matsumoto, N. Mondal, H. Yabu *et al.*, Study of ortho-positronium laser cooling, in *Proceedings of the 21st Beam Dynamics Workshop on Laser-Beam Interactions*, 2001.

[22] S. Aghion, C. Amsler, A. Ariga, T. Ariga, G. Bonomi, P. Bräunig, J. Bremer, R. S. Brusa, L. Cabaret, M. Caccia, R. Caravita, F. Castelli, G. Cerchiari, K. Chlouba, S. Cialdi, D. Comparat, G. Consolati, A. Demetrio, L. Di Noto *et al.*, Laser excitation of the $n = 3$ level of positronium for antihydrogen production, Phys. Rev. A **94**, 012507 (2016).

[23] C. Storry, A. Speck, D. Le Sage, N. Guise, G. Gabrielse, D. Grzonka, W. Oelert, G. Schepers, T. Sefzick *et al.*, First Laser-Controlled Antihydrogen Production, Phys. Rev. Lett. **93**, 263401 (2004).

[24] P. Yzombard, C. Amsler, T. Ariga, G. Bonomi, P. Bräunig, R. Brusa, L. Cabaret, M. Caccia, R. Caravita, F. Castelli *et al.*, Overview of recent work on laser excitation of positronium for the formation of antihydrogen, in *12th International Conference on Low Energy Antiproton Physics*, Vol. 18 (Kanazawa, Japan, 2017), p. 011026.

[25] M. Charlton, S. Eriksson, and G. M. Shore, *Antihydrogen and fundamental physics* (Springer, 2020).

[26] D. Cassidy, T. Hisakado, H. Tom, and A. Mills, Jr., Laser Excitation of Positronium in the Paschen-Back Regime, Phys. Rev. Lett. **106**, 173401 (2011).

[27] M. Anderson, J. Ensher, M. Matthews, C. Wieman, and E. Cornell, Observation of bose-einstein condensation in a dilute atomic vapor, Science **269**, 198 (1995).

[28] P. Yzombard, Laser cooling and manipulation of antimatter in the AEgIS experiment, PhD. thesis, Université Paris-Saclay, 2016.

[29] S. Curry, Combined zeeman and motional stark effects in the first excited state of positronium, Phys. Rev. A **7**, 447 (1973).

[30] C. Dermer and J. Weisheit, Perturbative analysis of simultaneous Stark and Zeeman effects on $n = 1 \leftrightarrow n = 2$ radiative transitions in positronium, Phys. Rev. A **40**, 5526 (1989).

[31] A. Alonso, B. Cooper, A. Deller, S. Hogan, and D. Cassidy, Positronium decay from $n = 2$ states in electric and magnetic fields, Phys. Rev. A **93**, 012506 (2016).

[32] A. Bartana, R. Kosloff, and D. Tannor, Laser cooling of internal degrees of freedom. II, J. Chem. Phys. **106**, 1435 (1997).

[33] H. Metcalf, Colloquium: Strong optical forces on atoms in multifrequency light, Rev. Mod. Phys. **89**, 041001 (2017).

[34] J. Bartolotta, M. Norcia, J. Cline, J. Thompson, and M. Holland, Laser cooling by sawtooth-wave adiabatic passage, Phys. Rev. A **98**, 023404 (2018).

[35] T. Chanelière, D. Comparat, and H. Lignier, Phase-space-density limitation in laser cooling without spontaneous emission, Phys. Rev. A **98**, 063432 (2018).

[36] X. Long, S. Scarlett, A. Jayich, and W. Campbell, Suppressed Spontaneous Emission for Coherent Momentum Transfer, Phys. Rev. Lett. **123**, 033603 (2019).

[37] Y. Tajima, K. Yamada, K. Shu, A. Ishida, S. Asai, M. Kuwata-Gonokami, E. Chae, and K. Yoshioka, Development of a sub-microsecond broadband pulsed laser for cooling positronium, In *CLEO: Applications and Technology* (Optical Society of America, 2020), pp. JTh2E–12.

[38] D. Comparat, Molecular cooling via Sisyphus processes, Phys. Rev. A **89**, 043410 (2014).

[39] The code has been developed under Code::Blocks (and Windows 64-bits) and is publicly available on https://github.com/dcompara/Laser-interaction-in-fields-rate-equations-forces.

[40] R. McConnell, G. Gabrielse, W. Kolthammer, P. Richerme, A. Müllers, J. Walz, D. Grzonka, M. Zielinski, D. Fitzakerley, M. George *et al.*, Large numbers of cold positronium atoms created in laser-selected Rydberg states using resonant charge exchange, J. Phys. B: At. Mol. Opt. Phys. **49**, 064002 (2016).

[41] S. Mariazzi, P. Bettotti, and R. Brusa, Positronium cooling and emission in vacuum from nanochannels at cryogenic temperature, Phys. Rev. Lett. **104**, 243401 (2010).

[42] S. Aghion, C. Amsler, M. Antonello, A. Belov, G. Bonomi, R. S. Brusa, M. Caccia, A. Camper, R. Caravita, F. Castelli, G. Cerchiari, D. Comparat, G. Consolati, A. Demetrio, L. Di Noto, M. Doser *et al.*, Producing long-lived 2^3s positronium via 3^3p laser excitation in magnetic and electric fields, Phys. Rev. A **98**, 013402 (2018).

[43] R. Caravita, S. Mariazzi, S. Aghion, C. Amsler, M. Antonello, A. Belov, G. Bonomi, R. S. Brusa, M. Caccia, A. Camper, F. Castelli, G. Cerchiari, D. Comparat, G. Consolati, A. Demetrio, L. Di Noto, M. Doser *et al.*, Positronium Rydberg excitation diagnostic in a 1t cryogenic environment, AIP Conf. Proc. **2182**, 030002 (2019).

[44] C. Amsler, M. Antonello, A. Belov, G. Bonomi, R. S. Brusa, M. Caccia, A. Camper, R. Caravita, F. Castelli, G. Cerchiari, D. Comparat, G. Consolati, A. Demetrio, L. Di Noto, M. Doser, M. Fanì, S. Gerber *et al.*, Velocity-selected production of 2^3S metastable positronium, Phys. Rev. A **99**, 033405 (2019).

[45] M. Rhee, Refined definition of the beam brightness, Phys. Fluids B **4**, 1674 (1992).

[46] C. Lejeune and J. Aubert, Emittance and brightness: Definitions and measurements, Adv. Electron. Electron Phys. Suppl. A 13, 159 (1980).

[47] C. Brau, What brightness means, in *The Physics and Applications of High Brightness Electron Beam, Proceedings of the ICFA Workshop* (Chia Laguna, Sardinia, 2002), p. 20.

[48] M. Reiser, *Theory and Design of Charged Particle Beams* (Wiley-VCH, Weinheim, 2008).

[49] E. Hessels, D. Homan, and M. Cavagnero, Two-stage Rydberg charge exchange: An efficient method for production of antihydrogen, Phys. Rev. A **57**, 1668 (1998).

[50] D. Krasnický, R. Caravita, C. Canali, and G. Testera, Cross section for Rydberg antihydrogen production via charge exchange between Rydberg positroniums and antiprotons in a magnetic field, Phys. Rev. A **94**, 022714 (2016).

[51] C. Amsler, M. Antonello, A. Belov, G. Bonomi, R. Brusa, M. Caccia, A. Camper, R. Caravita, F. Castelli, P. Cheinet, D. Comparat, G. Consolati, A. Demetrio, L. Di Noto, M. Doser, M. Fanì *et al.*, Pulsed production of antihydrogen, Commun. Phys. **4**, 19 (2021).

[52] H. K. Avetissian, A. K. Avetissian, and G. F. Mkrtchian, Self-Amplified Gamma-Ray Laser on Positronium Atoms from a Bose-Einstein Condensate, Phys. Rev. Lett. **113**, 023904 (2014).

[53] D. B. Cassidy, T. H. Hisakado, H. W. K. Tom, and A. P. Mills, Optical Spectroscopy of Molecular Positronium, Phys. Rev. Lett. **108**, 133402 (2012).

[54] H. Bethe and E. Salpeter, *Quantum Mechanics of One-and Two-Electron Atoms* (Springer Science & Business Media, Berlin, Heidelberg, 2012).

[55] S. Gerber, M. Doser, and D. Comparat, Pulsed production of cold protonium in Penning traps, Phys. Rev. A **100**, 063418 (2019).

[56] A. Pineda and J. Soto, Potential NRQED: The positronium case, Phys. Rev. D **59**, 016005 (1998).

[57] A. Alekseev, Two-photon annihilation of positronium in the p-state, Sov. Phys. JETP **7**, 856 (1958).

[58] A. Alekseev, Three-photon annihilation of positronium in the p-state, Sov. Phys. JETP **9**, 1312 (1959).

[59] A. Sen and Z. Silagadze, Two-photon decay of p-wave positronium: A tutorial, Can. J. Phys. **97**, 693 (2019).

[60] D. Varshalovich, A. Moskalev, and V. Khersonskii, *Quantum Theory of Angular Momentum*, (World Scientific, 1988).

[61] R. Caravita, Towards measuring gravity on neutral antimatter, Ph.D. thesis, Genoa University, 2017.

[62] T. Ida, M. Ando, and H. Toraya, Extended pseudo-Voigt function for approximating the Voigt profile, J. Appl. Crystallogr. **33**, 1311 (2000).

[63] D. Steck, *Quantum and Atom Optics*, http://atomoptics-nas.uoregon.edu/~dsteck/teaching/quantum-optics/, 2020.

[64] For more generality, we do not (yet) assume real dipoles and so the notation is different (care has to be taken though in the i, j order because $\Omega_{ji} = \Omega_{j\leftarrow i}$) to the one in Ref. [38].

[65] https://en.wikipedia.org/wiki/Euler_angles.

[66] S. Rajan, S. Wang, R. Inkol, and A. Joyal, Efficient approximations for the arctangent function, IEEE Signal Processing Mag. **23**, 108 (2006).

[67] M. Benammar, A. Alassi, A. Gastli, L. Ben-Brahim, and F. Touati, New fast arctangent approximation algorithm for generic real-time embedded applications, Sensors **19**, 5148 (2019).

[68] J.-M. Muller, Elementary functions and approximate computing, Proc. IEEE **108**, 2136 (2020).

[69] https://en.wikipedia.org/wiki/Wigner_D-matrix.

[70] In our case, we use the free implementations of the Mersenne twister unit-interval uniform random number generator of Matsumoto and Nishimura from GSL (GNU Scientific Library).